



# Short GRB Host Galaxies. I. Photometric and Spectroscopic Catalogs, Host Associations, and Galactocentric Offsets

Wen-fai Fong<sup>1</sup> , Anya E. Nugent<sup>1</sup> , Yuxin Dong<sup>1</sup> , Edo Berger<sup>2</sup> , Kerry Paterson<sup>3</sup> , Ryan Chornock<sup>4</sup> , Andrew Levan<sup>5</sup> , Peter Blanchard<sup>1</sup> , Kate D. Alexander<sup>1</sup> , Jennifer Andrews<sup>6</sup> , Bethany E. Cobb<sup>7</sup> , Antonino Cucchiara<sup>8</sup> , Derek Fox<sup>9</sup> , Chris L. Fryer<sup>10</sup> , Alexa C. Gordon<sup>1</sup> , Charles D. Kilpatrick<sup>1</sup> , Ragnhild Lunnan<sup>11</sup> , Raffaella Margutti<sup>4</sup> , Adam Miller<sup>1</sup> , Peter Milne<sup>12</sup> , Matt Nicholl<sup>13</sup> , Daniel Perley<sup>14</sup> , Jillian Rastinejad<sup>1</sup> , Alicia Rouco Escorial<sup>1</sup> , Genevieve Schroeder<sup>1</sup> , Nathan Smith<sup>12</sup> , Nial Tanvir<sup>15</sup> , and Giacomo Terreran<sup>16,17</sup>

<sup>1</sup> Center for Interdisciplinary Exploration and Research in Astrophysics (CIERA) and Department of Physics and Astronomy, Northwestern University, Evanston, IL 60208, USA; [wfong@northwestern.edu](mailto:wfong@northwestern.edu)

<sup>2</sup> Center for Astrophysics | Harvard & Smithsonian, 60 Garden St., Cambridge, MA 02138, USA

<sup>3</sup> Max-Planck-Institut für Astronomie (MPIA), Königstuhl 17, D-69117 Heidelberg, Germany

<sup>4</sup> Department of Astronomy, University of California, Berkeley, CA 94720-3411, USA

<sup>5</sup> Department of Astrophysics/IMAPP, Radboud University, 6525 AJ Nijmegen, The Netherlands

<sup>6</sup> Gemini Observatory/NSF's NOIRLab, 670 N. A'ohoku Pl., Hilo, HI 96720, USA

<sup>7</sup> Department of Physics, The George Washington University, Washington, DC 20052, USA

<sup>8</sup> College of Marin, Kentfield, CA 94904, USA

<sup>9</sup> Department of Astronomy & Astrophysics, The Pennsylvania State University, University Park, PA 16802, USA

<sup>10</sup> Center for Theoretical Astrophysics, Los Alamos National Laboratory, Los Alamos, NM, 87545, USA

<sup>11</sup> The Oskar Klein Centre, Department of Astronomy, Stockholm University, AlbaNova, SE-106 91 Stockholm, Sweden

<sup>12</sup> University of Arizona, Steward Observatory, 933 N. Cherry Ave., Tucson, AZ 85721, USA

<sup>13</sup> Birmingham Institute for Gravitational Wave Astronomy and School of Physics and Astronomy, University of Birmingham, Birmingham B15 2TT, UK

<sup>14</sup> Astrophysics Research Institute, Liverpool John Moores University, IC2, Liverpool Science Park, 146 Brownlow Hill, Liverpool L3 5RF, UK

<sup>15</sup> School of Physics and Astronomy, University of Leicester, University Rd., Leicester, LE1 7RH, UK

<sup>16</sup> Las Cumbres Observatory, 6740 Cortona Dr., Suite 102, Goleta, CA 93117-5575, USA

<sup>17</sup> Department of Physics, University of California, Santa Barbara, CA 93106-9530, USA

Received 2022 June 2; revised 2022 August 21; accepted 2022 September 11; published 2022 November 21

## Abstract

We present a comprehensive optical and near-infrared census of the fields of 90 short gamma-ray bursts (GRBs) discovered in 2005–2021, constituting all short GRBs for which host galaxy associations are feasible ( $\approx 60\%$  of the total Swift short GRB population). We contribute 274 new multi-band imaging observations across 58 distinct GRBs and 26 spectra of their host galaxies. Supplemented by literature and archival survey data, the catalog contains 542 photometric and 42 spectroscopic data sets. The photometric catalog reaches  $3\sigma$  depths of  $\gtrsim 24$ – $27$  mag and  $\gtrsim 23$ – $26$  mag for the optical and near-infrared bands, respectively. We identify host galaxies for 84 bursts, in which the most robust associations make up 56% (50/90) of events, while only a small fraction, 6.7%, have inconclusive host associations. Based on new spectroscopy, we determine 18 host spectroscopic redshifts with a range of  $z \approx 0.15$ – $1.5$  and find that  $\approx 23\%$ – $41\%$  of Swift short GRBs originate from  $z > 1$ . We also present the galactocentric offset catalog for 84 short GRBs. Taking into account the large range of individual measurement uncertainties, we find a median of projected offset of  $\approx 7.7$  kpc, for which the bursts with the most robust associations have a smaller median of  $\approx 4.8$  kpc. Our catalog captures more high-redshift and low-luminosity hosts, and more highly offset bursts than previously found, thereby diversifying the population of known short GRB hosts and properties. In terms of locations and host luminosities, the populations of short GRBs with and without detectable extended emission are statistically indistinguishable. This suggests that they arise from the same progenitors, or from multiple progenitors, which form and evolve in similar environments. All of the data products are available on the Broadband Repository for Investigating Gamma-Ray Burst Host Traits website.

*Unified Astronomy Thesaurus concepts:* [Stellar populations \(1622\)](#); [Gamma-ray bursts \(629\)](#); [Gravitational wave sources \(677\)](#)

*Supporting material:* figure set, machine-readable tables

## 1. Introduction

The host galaxies of astrophysical transients provide crucial insight into the nature of their progenitors. For instance, core-collapse supernovae (CCSNe), long-duration gamma-ray bursts (GRBs), and superluminous SNe are almost exclusively found to occur in star-forming galaxies (e.g., Savaglio et al. 2009;

Svensson et al. 2010; Li et al. 2011; Lunnan et al. 2014; Perley et al. 2016a; Schulze et al. 2021), helping to establish their progenitors as massive stars. The rate of these events thus traces recent star formation (e.g., Perley et al. 2016b). In contrast, Type Ia SNe originate in a mix of star-forming and quiescent galaxies (van den Bergh et al. 2005), consistent with an evolved progenitor and an event rate that traces both stellar mass and star formation (Sullivan et al. 2006).

Short-duration GRBs are relativistic explosions with prompt gamma-ray emission durations of  $\lesssim 2$  s (Kouveliotou et al. 1993), beaming-corrected total energy scales of  $\approx 10^{50}$  erg



Original content from this work may be used under the terms of the [Creative Commons Attribution 4.0 licence](#). Any further distribution of this work must maintain attribution to the author(s) and the title of the work, journal citation and DOI.

(Fong et al. 2015), and synchrotron afterglow radiation across the electromagnetic spectrum. Launched in 2004, NASA’s Neil Gehrels Swift Observatory (Gehrels et al. 2004) has served as the primary workhorse for short GRB discovery and precise localization. The detection of X-ray afterglows allows Swift to localize  $\approx 70\%$  of short GRBs which it discovers within just a few arcseconds, resulting in  $\sim 8$  such short GRBs per year (Lien et al. 2016). Critically, these localizations enable robust associations between GRBs and their host galaxies. With host galaxies, one can discern fundamental properties such as redshifts and burst energy scales, as well as properties of the environment on sub-galactic to kiloparsec scales.

The locations of transients with respect to their host galaxies also provide crucial diagnostics into their origins. While transients originating from massive stars (long GRBs, CCSNe, SLSNe) are typically located in or proximal to regions of active star formation (Fruchter et al. 2006; Kelly et al. 2008; Lunnan et al. 2015; Blanchard et al. 2016; Lyman et al. 2017; Audcent-Ross et al. 2020), short GRBs often occur several kiloparsecs from their host galaxies, with locations only weakly correlated with the stellar light distributions of their hosts (Berger 2010; Fong & Berger 2013; Tunnicliffe et al. 2014; Zevin et al. 2020; O’Connor et al. 2022). Moreover, high angular resolution observations have revealed weak correlations between short GRB locations and the distributions of their host stellar mass or star formation (Fong & Berger 2013). These studies provide some of the most compelling indirect evidence to date that their progenitors migrate from their birth sites to explosion sites, matching the hallmark prediction of binary neutron star (BNS) and neutron star-black hole (NSBH) mergers (Fryer et al. 1999).

With the 2017 joint detection of the BNS merger GW170817 in conjunction with a short GRB, we now have direct evidence that BNS mergers are the progenitors of at least some short GRBs (Abbott et al. 2017a; Goldstein et al. 2017; Savchenko et al. 2017; Margutti & Chornock 2021). With the ground-breaking discoveries of the first definitive BNS mergers provided by gravitational wave (GW) facilities (Abbott et al. 2017b, 2020a), and the promise of more to come in the very near future (Abbott et al. 2020b), it is especially timely to perform a uniform and careful study of Swift short GRB environments, which serve as a cosmological comparison data set out to a redshift of  $z \approx 2.5$  (Berger 2014; Selsing et al. 2018; Paterson et al. 2020; O’Connor et al. 2022). At present, there is heightened interest in short GRBs, their inference on heavy element nucleosynthesis, and the crucial role they play in understanding the evolution of mergers over cosmic time.

The existing sample of cosmological short GRB ( $z \approx 0.1\text{--}2.5$ ) is much larger than the two confirmed BNS merger detections from GWs to date (Abbott et al. 2017b, 2020a), and it will be many years before GW-detected mergers yield a comparable sample of well-localized events based on expected rates (Abbott et al. 2019). Aside from GW events, nearly all of our observational constraints on BNS systems originate from the  $\sim 19$  known Galactic BNS systems (Willems et al. 2004; Wong et al. 2010; Tauris et al. 2017; Vigna-Gómez et al. 2018), a population that suffers from various selection biases. For instance, it is challenging to identify tight (short delay time) Galactic BNS systems due to signal smearing, as well as systems with large orbital separations (long delay times) due to the small relative changes in proper motions (Tauris et al. 2017). On the other hand, short

GRBs are detected to cosmological redshifts via gamma-ray emission, and represent a large and complementary data set of merging systems. Thus, to fully understand how BNS/NSBH binaries form and merge across cosmic history, and to provide a legacy comparison data set for future GW events, it is critical to identify and characterize the host galaxies of as many short GRBs as possible.

The first decade of short GRB host galaxy studies primarily concentrated on those bursts with subarcsecond localizations via the detection of optical afterglows (Fox et al. 2005; Villasenor et al. 2005; Berger et al. 2007; D’Avanzo et al. 2009; Fong et al. 2013; Berger 2014; De Pasquale 2019). However, the selection based on optical afterglows may bias the host galaxy sample and interpretation for their progenitors, as has been shown for long GRB hosts (e.g., Hjorth et al. 2012). Now, we are well into the second decade of afterglow discoveries, and are equipped with over 100 short GRBs localized primarily by X-ray afterglows.

Here, we present a comprehensive census of the locations and environments of the Swift short GRB population, representing a decade-long observational campaign to identify and characterize as many short GRB host galaxies as possible, irrespective of the detection of an optical afterglow. This work represents the first of a series of two papers. Paper I focuses on the photometric and spectroscopic catalogs, host galaxy associations, spectroscopic redshifts, and galactocentric offsets. Paper II, Nugent et al. (2022), focuses on spectral energy distribution (SED) modeling of these data, their inferred stellar population properties, and implications for the progenitors. We house all of the data and modeling products in these works on the Broadband Repository for Investigating Gamma-ray burst Host Traits (BRIGHT) website.<sup>18</sup>

In Section 2, we describe our sample of 90 events. In Section 3, we introduce 274 photometric observations across 58 distinct short GRBs taken with 4–10 m ground-based telescopes, the Hubble Space Telescope (HST) and the Spitzer Space Telescope. In Section 4, we describe the process for host association and report associations to 84 events with varying degrees of robustness. In Section 5, we present 26 spectroscopic observations of short GRB hosts and redshifts for 18 events. In Section 6, we report the galactocentric offsets for 84 events (angular, physical, and host normalized when available), and compare the distributions to long GRBs and NS merger models. We discuss the implications of the results, selection effects, and assessment of contamination to our sample in Section 7. We conclude in Section 8.

Unless otherwise stated, all observations are reported in the AB magnitude system and have been corrected for Galactic extinction in the direction of the GRB (Schlafly & Finkbeiner 2011) and employed the Cardelli et al. (1989) extinction law. We employ a standard cosmology of  $H_0 = 69.6 \text{ km s}^{-1} \text{ Mpc}^{-1}$ , and  $\Omega_M = 0.286$ ,  $\Omega_{\text{vac}} = 0.714$  (Bennett et al. 2014).

## 2. Sample Description

We begin with all short GRBs discovered by NASA’s Swift Observatory (Gehrels et al. 2004) since its launch in 2004, as well as two short GRBs discovered by the High Energy Transient Explorer (HETE-2; Ricker et al. 2003), but with  $\lesssim 1''$  localizations via the detection of afterglows (GRBs 050709 and 060121). We include events that meet both of the following

<sup>18</sup> <http://bright.ciera.northwestern.edu>

criteria: (i) GRBs with Swift gamma-ray durations of  $T_{90} \leq 2$  s (15–350 keV) or those that are classified as short or possibly short with extended emission (short GRB-EE; according to Norris & Bonnell 2006; Lien et al. 2016), and (ii) bursts with detected afterglows with  $\lesssim 5''$  radius precision, which typically enable associations to host galaxies. Such afterglow discoveries primarily come from the Swift X-ray Telescope (XRT), which routinely provides localizations of  $\approx 2''$ – $5''$  in radius (90% confidence; Evans et al. 2009), as well as ground-based optical facilities and the Chandra X-ray Observatory (CXO). We note that by using observable, as opposed to rest-frame quantities, we are able to be inclusive of the sizable fraction of bursts with unknown redshift. We note that we explore possible selection effects and contamination in Section 7.

We additionally include three events that nominally have long durations but likely do not originate from massive star progenitors: GRBs 060614, 160303A, and 211211A. GRB 060614 has  $T_{90} = 108.7$  s and is classified as a possible short GRB-EE (Lien et al. 2016), with a spectral lag and gamma-ray luminosity completely consistent with the short-hard GRB population (Gehrels et al. 2006; Lien et al. 2016). Additionally, with the lack of associated SN to deep limits, there is a general consensus that this event did not originate from a massive star collapse (Della Valle et al. 2006; Fynbo et al. 2006; Gal-Yam et al. 2006). Moreover, there is tentative evidence for a photometric excess interpreted as a kilonova (Jin et al. 2015). Thus, we include this burst in our sample. The Swift/BAT light curve of GRB 160303A exhibits a  $\sim 0.4$  s spike followed by a low-significance tail to  $\sim 5$  s, with a spectral lag of (measured in the 100–350 keV to 25–50 keV bands) of  $24 \pm 24$  ms, yielding inconclusive results as to its classification from the gamma-ray properties alone (Ukwatta et al. 2016). However, the lack of clear emission lines from the host galaxy in its afterglow spectrum (de Ugarte Postigo et al. 2016), coupled with its large offset (Section 6.2) indicate a GRB with an older stellar progenitor, and we thus include this burst in our sample. Finally, GRB 211211A has  $T_{90} \approx 51.4$  s and is in the long GRB class based on its gamma-ray hardness and duration. However, this event was followed by near-infrared (NIR) transient emission interpreted as an  $r$ -process kilonova and also has deep limits on an associated SN. Taken together, this event likely originated from an NS merger (Rastinejad et al. 2022). Including these three bursts, there are 107 events discovered during 2004–2021 that meet the criteria for our starting sample.

From this sample, we exclude 17 short GRBs with sightlines that are subject to observing constraints that prevent meaningful host galaxy follow-up. Such constraints include significant contamination of the afterglow position by a foreground star, high-extinction sightlines from the Galaxy ( $A_V \gtrsim 2$  mag; Schlafly & Finkbeiner 2011), or crowded fields. Thus, our starting sample of 90 short GRBs with positions and sightlines that enable host galaxy searches and follow-up corresponds to  $\approx 60\%$  of the total Swift population (Figure 1).

### 3. Photometric Catalog and Observations

The first goal of our study is to build a multi-band photometric catalog for the locations of the 90 short GRBs in the sample in order to identify new host galaxies or confirm previously reported ones. Once we establish a host galaxy, we obtain imaging in multiple filters and/or spectroscopy (Section 5) to characterize their SEDs. The photometric part

of the catalog is comprised of ground-based, HST and Spitzer/IRAC observations, supplemented by published literature and archival survey data. Here, we describe the imaging data in the catalog, data reduction, and photometric methods.

In total, we newly contribute 274 observations in various bands across 58 distinct short GRBs. We supplement this with literature and archival data for a total of 542 photometric data points and imaging products across 90 events in the photometric catalog. The photometry and host galaxy positions are listed in Table A1.

#### 3.1. Ground-based Imaging for Host Galaxy Searches

We first present new ground-based data for events in our sample that were discovered since the launch of Swift in 2004 until 2021 December. We attempted a photometric host galaxy search for every short GRB discovered during these years, except for those that have already published identified hosts, are difficult to access with our telescope resources, or have observing constraints that would prevent a meaningful search. In some cases for bursts with published hosts, we obtained imaging in complementary filters to characterize the host SEDs.

To search for host galaxies, we initiated an initial round of deep ground-based imaging for 58 bursts. In general, we obtained optical imaging centered on the most precise available afterglow position in the  $r$  or  $i$  band. If this imaging did not yield a plausible host galaxy candidate at or proximal to the afterglow position, we obtained NIR imaging in the  $J$  or  $K$  bands to search for a reddened host (potentially due to a dusty or higher-redshift origin). If either set of optical or NIR initial imaging revealed a plausible host galaxy (see Section 4.2), we obtained 1–10 bands of additional multi-band observations in any of the  $ugriz$ ,  $UVRI$ ,  $RG850$ ,  $YJHK$ , or  $K_s$  filters to characterize the putative host galaxy SED. If neither our optical nor NIR imaging yielded a plausible host galaxy, we used these ground-based limits to place constraints on the luminosity and redshift of spatially coincident hosts. For five of these events, we obtained follow-up HST observations to perform a more sensitive search for spatially coincident hosts (Section 3.3).

We obtained these observations with the twin 6.5 m Magellan/Baade and Clay telescopes (PIs: Berger, Blanchard), 8 m Gemini-North and Gemini-South telescopes (PIs: Fong, Cucchiara), 6.5 m MMT (PIs: Fong, Nugent), twin 10 m Keck I and II telescopes (PIs: Paterson, Fong, Terreran, and Miller), the 3.8 m United Kingdom InfraRed Telescope (UKIRT; PI: Fong), and the twin 8.4 m Large Binocular Telescopes (LBT; PI: Fong, Smith). We used 18 distinct instruments across these facilities for imaging. The telescopes, instruments, and filters used for our catalog are listed in Table 1. This imaging typically reaches  $3\sigma$  limits of  $m_{AB,opt} \gtrsim 24$ – $26$  mag and  $m_{AB,NIR} \gtrsim 22$ – $23.5$  mag.

For data reduction and co-addition, we use a combination of standard tasks in the IRAF/ccdred package (Tody 1986; for Magellan, LBT, MMT/MMTCam data), observatory-specific pipelines (for Gemini data), and the POTPyRI software<sup>19</sup> (for Keck, MMT/Binospec and MMIRS data). For optical data, we apply bias corrections, flat-field corrections using either dome or twilight flats, and dark current corrections when relevant. For NIR data, we additionally apply sky subtraction using coeval on-sky frames. For UKIRT/WFCAM data, we obtain preprocessed images from the WFCAM Science Archive

<sup>19</sup> <https://github.com/CIERA-Transients/POTPyRI>

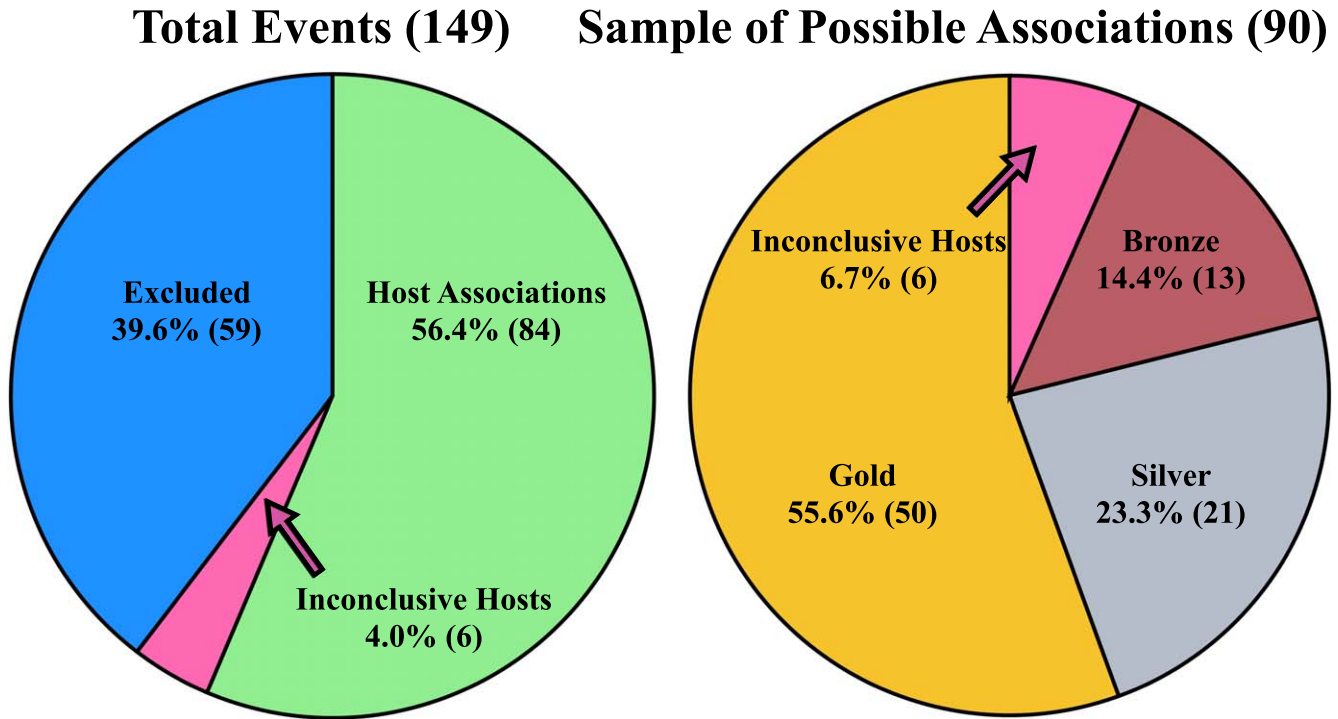


**Figure 1.** Left: classification of all short GRBs in the starting sample of short GRBs primarily discovered by Swift. Of the 149 total detected Swift short GRBs, host associations exist for  $\approx 56\%$  of the population, while only  $\approx 4\%$  have inconclusive hosts. We exclude  $\approx 40\%$  of the total population because they have no reported afterglows, afterglow localizations too large to enable meaningful host galaxy searches, or are events that are subject to optical observing constraints. Right: classification of the 90 short GRBs in our sample for which meaningful host searches and follow-up are feasible. We report host associations for  $\approx 93.3\%$  of events (84); the most robust associations ( $P_{\text{cc,min}} \lesssim 0.02$ ) comprise over half of events (Gold sample). We cannot make conclusive host associations ( $P_{\text{cc,min}} \gtrsim 0.25$ ) for  $\approx 6.7\%$  of events.

(Hamly et al. 2008), which are already corrected for bias, flat field, and dark current by the Cambridge Astronomical Survey Unit.<sup>20</sup> For each epoch and filter, we co-add the images and perform astrometry relative to Two Micron All Sky Survey (2MASS) using a combination of tasks in Starlink<sup>21</sup> and IRAF. The full listing is available in Appendix A and the BRIGHT website.<sup>22</sup> The images are shown in Figures 2 and 3.

### 3.2. HST Observations

We supplement the ground-based imaging with HST observations for 10 events, consisting of events that we have not yet analyzed in our previous works. Six GRBs were imaged in a single band with the F110W filter using the infrared channel on the Wide-Field Camera 3 (WFC3/IR) under Program 14685 (PI: Fong). The purpose of this program was to search for redder host galaxies that may have gone undetected from ground-based optical observations. Indeed, at the time of observation, five of these events had no reported or detected host galaxy at their subarcsecond optical afterglow positions to the limits of ground-based imaging (GRBs 091109B, 110112A, 130912A, 131004A, and 150423A). We recover plausible host galaxies for three of these events (Section 4.2). The sixth event observed in F110W, GRB 160303A, had a ground-based GTC detection of a possible host galaxy (Cano et al. 2016), and this is well detected in our HST imaging (Figure 2). These HST data also newly appear in O’Connor et al. (2022).

The four additional events have multiple epochs and filters (GRBs 060614, 150424A, 160624A, and 160821B) under Programs 10917 (PI: Fox), 13830, 14237 (PI: Tanvir), and 14357 (PI: Troja), and were previously published (Gal-Yam et al. 2006; Knust et al. 2017; Jin et al. 2018; Lamb et al. 2019a; Troja et al. 2019; O’Connor et al. 2021; Rastinejad et al. 2021). For each of these latter events, we select the filter that yields the highest signal-to-noise ratio (S/N) for sources in the image to perform our subsequent analysis.

For data reduction, we retrieved preprocessed images from the HST archive<sup>23</sup> for observations of these nine short GRBs. We used the *astrodrizzle* routine as part of the *drizzlepac* package in PyRAF to apply standard distortion corrections and combine the exposures for each event and filter. For WFC3/IR imaging, we use  $\text{pixfrac} = 0.8$  and  $\text{pixscale} = 0''.0642 \text{ pixel}^{-1}$ , half of the native pixel scale. For WFC3/UVIS images, we first apply a charge transfer efficiency (CTE) correction using the stand-alone Fortran program,<sup>24</sup> and then use *astrodrizzle* to combine the CTE-corrected exposures using  $\text{pixscale} = 0''.033 \text{ pixel}^{-1}$ . For the ACS images, we use  $\text{pixfrac} = 1.0$  and  $\text{pixscale} = 0''.05 \text{ pixel}^{-1}$ . The images are shown in Figure 2.

We also compile available photometric data and reduced imaging for all remaining short GRBs with HST observations from our previous works. This results in the addition of 26 short GRBs with HST data. These bursts and their references are listed in Table 2 and Table A1.

<sup>20</sup> <http://casu.ast.cam.ac.uk/>

<sup>21</sup> <http://starlink.eao.hawaii.edu/starlink>

<sup>22</sup> <https://bright.ciera.northwestern.edu/>

<sup>23</sup> <https://archive.stsci.edu/hst/>

<sup>24</sup> [http://www.stsci.edu/hst/wfc3/tools/cte\\_tools](http://www.stsci.edu/hst/wfc3/tools/cte_tools)

**Table 1**  
Telescopes, Instruments, Photometric, or Spectroscopic Setups

Telescope	Instrument	Mode	Setups or Filters
Gemini-South	Gemini Multi-Object Spectrograph (GMOS)	Imaging	<i>griz</i>
		Spectroscopy	<i>R400, B600</i>
Gemini-North	FLAMINGOS-2	Spectroscopy	<i>JH</i>
	Gemini Multi-Object Spectrograph (GMOS)	Imaging	<i>griz</i>
		Spectroscopy	<i>R400, B600</i>
Keck I	Near-Infrared Imager	<i>JHK</i>	
	Low Resolution Imaging Spectrometer (LRIS)	Imaging	<i>GRI, RG850</i>
		Spectroscopy	<i>400/3400, 400/8500</i>
Keck II	Multi-Object Spectrometer For Infra-Red Exploration (MOSFIRE)	Imaging	<i>YJHK<sub>s</sub></i>
Large Binocular Telescope	DEep Imaging Multi-Object Spectrograph (DEIMOS)	<i>VRIZ</i>	
	Large Binocular Camera (LBC)	<i>ugriz</i>	
Magellan Baade	Multi-Object Double CCD Spectrographs (MODS1, MODS2)	<i>ugriz</i>	
	Inamori Magellan Areal Camera and Spectrograph (IMACS)	f/2 Imaging	<i>griz</i>
Magellan Clay	FourStar	f/2 Spectroscopy	<i>200/15.0, 300/17.5, 300/26.7</i>
		Imaging	<i>JHK<sub>s</sub></i>
	Low Dispersion Survey Spectrograph 3 (LDSS3)	Imaging	<i>griz</i>
		Spectroscopy	<i>VPH-ALL</i>
MMT	Persson's Auxiliary Nasmyth Infrared Camera (PANIC)	<i>JK<sub>s</sub></i>	
	Binospec	Imaging	<i>griz</i>
		Spectroscopy	<i>2701</i>
United Kingdom InfraRed Telescope	MMTCam	Imaging	<i>gri</i>
	Magellan Infrared Spectrograph (MMIRS)	Imaging	<i>YJHK</i>
	Wide Field Camera (WFCAM)	Imaging	<i>YJHK</i>
	UKIRT Fast-Track Imager (UFTI)	Imaging	<i>JHK</i>
Hubble Space Telescope (HST)	Wide Field Survey Camera 3 (WFC3)	Imaging	<i>F814W, F110W, F160W</i>
	Advanced Camera for Surveys (ACS)	Imaging	<i>F606W</i>
Spitzer Space Telescope (Spitzer)	Infrared Array Camera (IRAC)	Imaging	<i>Channels 1, 2, 3, 4</i>

**Note.** Telescope, instrument suites, imaging filters, and spectroscopic gratings and grisms used in the new host galaxy data presented in this paper (Section 3 and Section 5). Literature or archival data that supplement this sample comprise a larger variety of telescopes and instruments not listed here.

### 3.3. Spitzer Space Telescope Observations

Observations from IRAC (Fazio et al. 2004) on the Spitzer Space Telescope (Werner et al. 2004) were available for 13 of the GRB host galaxies in our sample taken during 2006–2017<sup>25</sup> (PIs: Perley, Savaglio, Gladders). We obtained the Level 2 PBCD mosaic images from the Spitzer Heritage archive for these fields and deblended the GRB host from its (apparent) companions using the interactive Galfit-based modeling method detailed in Perley et al. (2016c). For host galaxies smaller than 1'' we measure the host galaxy magnitude on the companion-subtracted image using a custom IDL aperture photometry routine using a 2.''4 aperture and a 3.''6–4.''8 background annulus fixed at the GRB host location from Table 2, with a custom aperture correction calculated using the Spitzer-supplied point-response function model. (The photometric scale is taken from the PBCD images, which have already been flux calibrated.) For two cases (GRBs 050509B and 050724A), we use a larger source aperture of 4.''8 as the smaller aperture does not adequately encompass the source flux. The results are presented in Table A1. In the case of a non-detection, the quoted limit corresponds to 5 $\sigma$  confidence.

### 3.4. Literature or Archival Survey Photometry

To supplement these observations, we draw from published ground-based data in the literature, focusing on (i) previously published, well-characterized hosts, or (ii) hosts that lack

imaging in a given filter in our catalog. In this vein, we collect literature photometry for 44 bursts. We list the references for all of these data in Table 2. When made available by corresponding authors, we also provide the reduced stacks from these works on the BRIGHT website. We emphasize that the literature data set is comprehensive for a given host in that we attempt to fill out the SED, but does not include all literature photometry that exists for every host galaxy.

Finally, for 10 bursts, we include archival photometric survey data. We draw from Two Micron All Sky Survey All-Sky (2MASS; Skrutskie et al. 2006), Legacy Surveys Data Release 9 (DR 9; Dey et al. 2019), Pan-STARRS Data Release (DR2; Flewelling et al. 2020), Sloan Digital Sky Survey Data Release 12 (SDSS DR12; Alam et al. 2015), SDSS DR13, (Albareti et al. 2017), Spitzer (Papovich et al. 2016; Timlin et al. 2016), and Wide-field Infrared Survey Explorer (WISE; Lang et al. 2016).

### 3.5. Afterglow Observations

To obtain afterglow positions and thus burst locations with respect to putative host galaxies, we first use ground-based optical discovery images when available. In particular, we utilize a combination of our Target-of-Opportunity programs on the twin 6.5 m Magellan telescopes, the 6.5 m MMT, the twin Gemini telescopes, and the 60 in Palomar Observatory P60 telescope (PIs: Berger, Fong, Cenko, Cucchiara), as well as publicly available ground-based imaging from the 4.2 m William Herschel Telescope and the 8.2 m Very Large Telescope (VLT). For all ground-based observations, we use

<sup>25</sup> There were also observations available for GRBs 150120A and 161001A but severe blending from nearby sources inhibited accurate photometry.

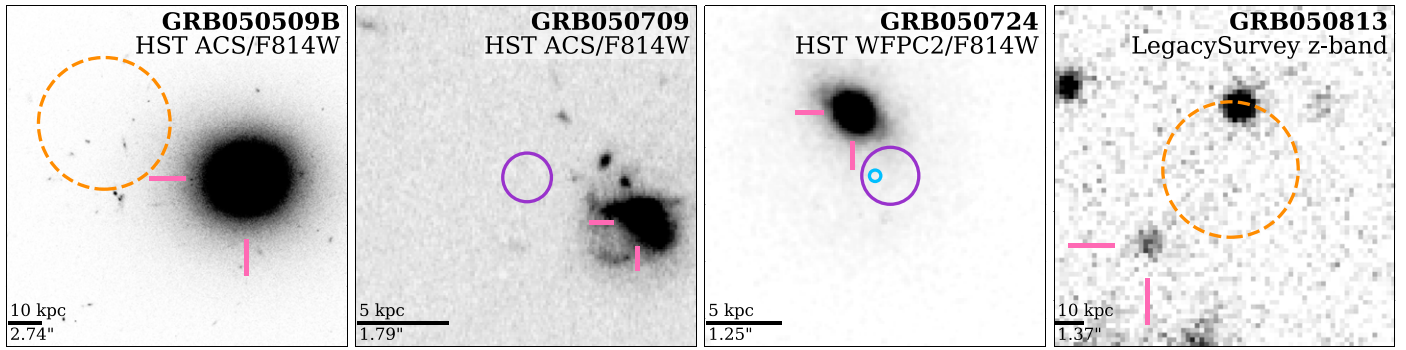


**Figure 2.** Representative images of the host galaxies of the short GRBs in our catalog. In each panel, the most precise afterglow localization(s) for each burst is/are plotted (XRT 90%: orange dashed, optical  $1\sigma$ : blue, Chandra or VLA  $1\sigma$ : purple). The putative host galaxy is denoted by the pink crosshairs. All images are oriented north up and east to the left. The complete figure set (90 images) is available in the online journal.

(The complete figure set (90 images) is available.)

the same procedures for data reduction as for our host galaxy imaging, described in Section 3.

For the subset of bursts for which there exists HST afterglow discovery imaging, we retrieve and process the images as described in Section 3.3. For both ground-based and HST imaging, if the position of the afterglow is contaminated by host galaxy light in the discovery image, we use the HOTPANTS software package (Becker 2015) to perform image subtraction between the afterglow images and late-time templates to produce residual images for accurate afterglow centroiding. We use Source Extractor (SExtractor; Bertin & Arnouts 1996) to determine the positional uncertainties of the afterglows,  $\sigma_{\text{GRB}}$ . We calculate a range of  $\sigma_{\text{GRB}} \approx 10\text{--}120$  mas for ground-based discoveries, and  $\sigma_{\text{GRB}} \approx 1\text{--}4$  mas for bursts with HST-detected afterglows.

For bursts for which the most precise afterglow localization is from the CXO, we retrieve Level II files from the Chandra archive, and we use CIAO/wavdetect to determine their positions and uncertainties. We describe how relative astrometry is performed to the host galaxy images in Section 4.1. For afterglows detected with the Karl G. Jansky Very Large Array (VLA) or Atacama Large Millimeter Array, we use CASA/jmfit to fit a 2D Gaussian to the afterglow. Finally, for 33 bursts, the most precise afterglow localization is from Swift/XRT. In these cases, we use the published positions and uncertainties,<sup>26</sup> with the methods described in Evans et al. (2009).

## 4. Host Galaxy Associations

### 4.1. Astrometry

For each host galaxy stack, we perform absolute astrometry using common sources between the host galaxy imaging and available source catalogs: Gaia DR2 (Gaia Collaboration et al. 2018), Pan-STARRS (PS1; Chambers et al. 2016), SDSS DR12 (Alam et al. 2015), or 2MASS. We use SExtractor to determine the centroids of common sources, and IRAF/ccred and ccsetwcs to determine the astrometric solution from each image to the catalog. We find that a fourth-order polynomial with six free parameters corresponding to a shift, scale, and rotation in each coordinate provides robust solutions. The  $1\sigma$  absolute astrometric uncertainties have a range of  $\sigma_{\text{abs}} \approx 0''.1\text{--}0''.3$ . We report the host galaxy positions in Table A1.

<sup>26</sup> We draw the positions and uncertainties from [https://www.swift.ac.uk/xrt\\_positions/](https://www.swift.ac.uk/xrt_positions/), using values as of 2022 June.

In order to make host galaxy identifications, it is necessary to align the afterglow and host galaxy imaging to the same frame. Thus, we additionally perform relative astrometry from the available afterglow imaging (from ground-based facilities, HST, or CXO) to the host galaxy images, which themselves are tied to an absolute astrometric system. We again use a combination of SExtractor and IRAF using common sources. The  $1\sigma$  uncertainty on the afterglow position includes the afterglow positional uncertainty (see Section 3.5) and the relative astrometric tie uncertainty ( $\sigma_{\text{rel}} \approx 10\text{--}100$  mas) added in quadrature. If we do not have access to afterglow discovery images, we use published positions from the literature or GCNs. If uncertainties are not provided with those positions, we assume a conservative  $1\sigma$  uncertainty of  $0''.5$ . For the 33 bursts with no subarcsecond localization, and X-ray positions only from Swift/XRT, we use the published XRT positions directly (typically  $\approx 1''.5\text{--}5''$ ; Evans et al. 2009). For 89 of the 90 fields, we show a representative, deep optical or NIR image centered on the most precise afterglow position for each burst in Figures 2 and 3.<sup>27</sup>

### 4.2. Probability of Chance Coincidence

We use the available imaging data to determine the most probable host galaxy for each burst by calculating the probability of chance coincidence ( $P_{\text{cc}}$ ) for nearby galaxies in the field of view. The fields of view are typically  $>2''.5$  in radius, corresponding to  $\approx 1$  Mpc at  $z = 0.5$ . For context, the largest observed projected physical offsets for short GRBs are only  $\lesssim 100$  kpc (Berger 2010; Tunnicliffe et al. 2014). The  $P_{\text{cc}}$  method requires two ingredients: angular offsets between a host galaxy candidate and burst location,  $\delta R$ , and putative host galaxy magnitudes,  $m_i$ . The methods to calculate  $\delta R$  are described in Section 6.

Using our deepest available image for each burst, which is typically in the  $r$  band or  $JH$  bands, we start with the extended source that has the smallest angular offset to the most precise afterglow position. For this source, we perform aperture photometry using the IRAF/apphot package. We begin with default apertures of  $2.5\theta_{\text{FWHM}}$ , but often use larger apertures to fully encompass the galaxy light. For background regions, we use annuli immediately surrounding the putative hosts, and

<sup>27</sup> We only lack imaging for GRB 081226A and use the results reported in Nicuesa Guelbenzu et al. (2012) for our subsequent analysis.

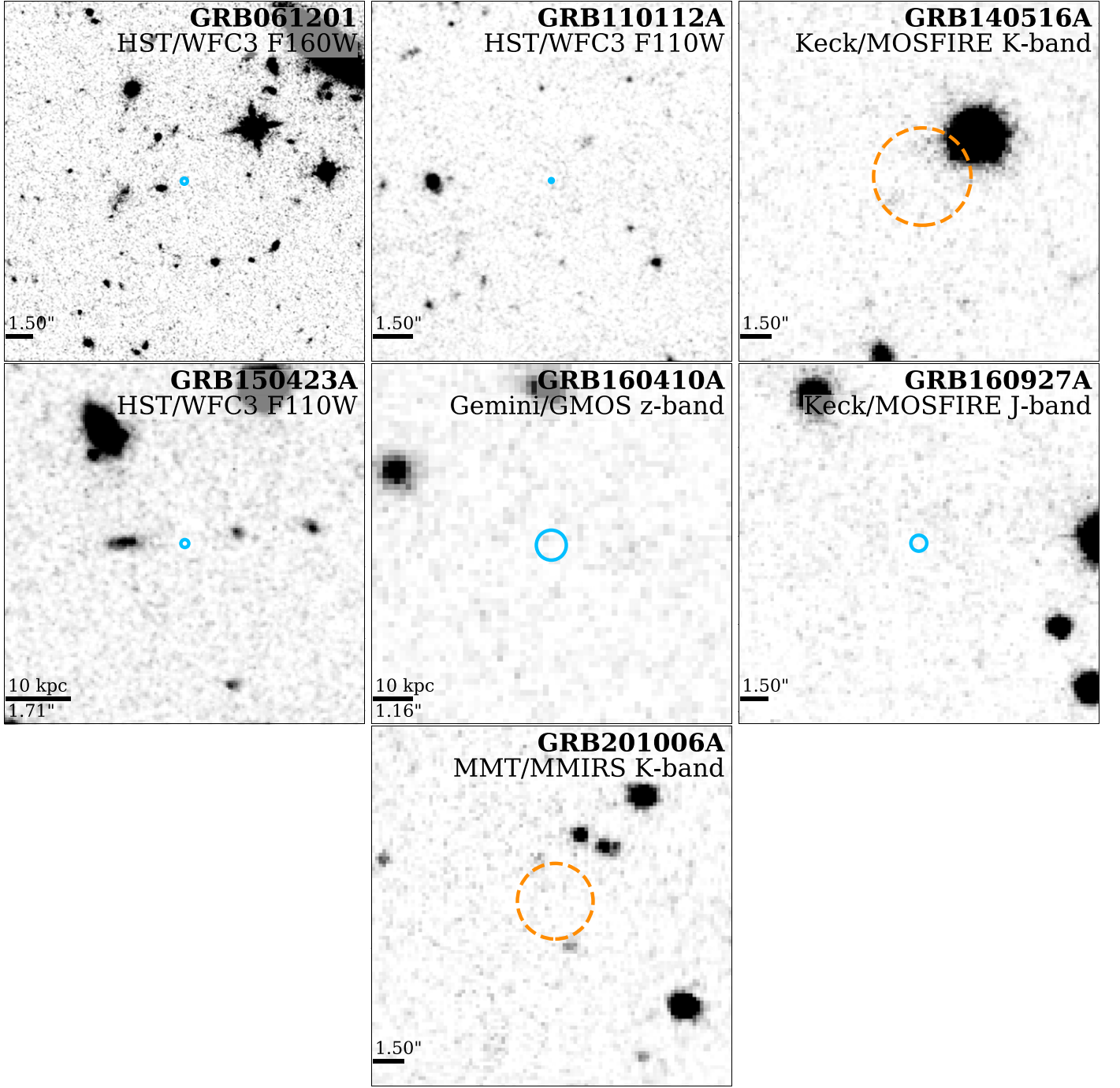


**Figure 3.** The fields of six short GRBs with no clear host association ( $P_{\text{cc,min}} \gtrsim 0.25$ ), classified as “Inconclusive” associations. Orange dashed circles are XRT positions, while solid blue circles are optical positions. Also displayed is the field of GRB 201006A, which has a high-extinction sightline of  $A_V = 3.5$  mag (falling in the observing constraint category), but for which we have deep  $K$ -band imaging to place limits on a redder host. These images reach  $3\sigma$  depths of  $\gtrsim 26$ – $28$  mag on coincident host galaxies.

adjust the radii as needed to avoid any contaminating sources. We determine zero points either by using stars with cataloged magnitudes in the field of the host galaxy, or by using standard star fields taken on the same night at similar airmasses. For the determination of optical zero points, we use SDSS DR12, Pan-STARRS (applying transformations to the SDSS system; Tonry et al. 2012), or the USNO-B catalogs. For NIR zero points, we use the 2MASS catalog. When relevant, we convert from the Vega to the AB system, using standard transformations or instrument-specific conversions. For HST data, we use the

relevant tabulated zero point for each instrument and filter,<sup>28</sup> again varying the apertures and background regions based on the size of each galaxy.

We follow the methodology of Bloom et al. (2002) to calculate  $P_{\text{cc}}$  based on the surface density of galaxies brighter than a given magnitude,  $\sigma(\leq m_i)$  within a radius,  $R_i$ . To determine  $\sigma(\leq m_i)$ , we interpolate  $r$ -band or  $H$ -band number

<sup>28</sup> [http://www.stsci.edu/hst/wfc3/ir\\_phot\\_zpt](http://www.stsci.edu/hst/wfc3/ir_phot_zpt) and <https://acszeropoints.stsci.edu/>.

**Table 2**  
Short Gamma-Ray Burst Host Galaxy Sample

GRB	R.A. (J2000)	Decl. (J2000)	Redshift	Filter	$m_{AB}$ (AB mag)	$P_{cc}$	Class	References
050509B	12 <sup>h</sup> 36 <sup>m</sup> 12 <sup>s</sup> .875	+28°58′ 58″.84	0.2248 ± 0.0002	<i>r</i>	17.123 ± 0.01	5 × 10 <sup>−3</sup>	Gold	1–4
050709	23 <sup>h</sup> 01 <sup>m</sup> 26 <sup>s</sup> .765	−38°58′ 40″.422	0.1607 ± 0.0004	<i>R</i>	21.258 ± 0.07	3 × 10 <sup>−3</sup>	Gold	2, 5–8
050724	16 <sup>h</sup> 24 <sup>m</sup> 44 <sup>s</sup> .410	−27°32′ 26″.393	0.254 ± 0.001	<i>R</i>	19.829 ± 0.03	2 × 10 <sup>−5</sup>	Gold	2, 9–10
050813	16 <sup>h</sup> 07 <sup>m</sup> 57 <sup>s</sup> .200	+11°14′ 53″.09	0.719 ± 0.001	<i>R</i>	23.43 ± 0.07	0.2	Bronze	11–13
051210	22 <sup>h</sup> 00 <sup>m</sup> 40 <sup>s</sup> .942	−57°36′ 47″.063	2.58 <sup>+0.11</sup> <sub>−0.17</sub>	<i>r</i>	24.043 ± 0.15	0.04	Silver	2, 8, This work
051221A	21 <sup>h</sup> 54 <sup>m</sup> 48 <sup>s</sup> .653	+16°53′ 27″.335	0.5464 ± 0.0001	<i>r</i>	22.178 ± 0.09	5 × 10 <sup>−5</sup>	Gold	2, 8, 14
060121	09 <sup>h</sup> 09 <sup>m</sup> 52 <sup>s</sup> .026	+45°39′ 45″.538	...	F606W	26.27	2 × 10 <sup>−3</sup>	Gold	2
060313	04 <sup>h</sup> 26 <sup>m</sup> 28 <sup>s</sup> .402	−10°50′ 39″.901	...	F475W	26.68	3 × 10 <sup>−3</sup>	Gold	2
060614 <sup>c</sup>	21 <sup>h</sup> 23 <sup>m</sup> 32 <sup>s</sup> .102	−53°01′ 36″.436	0.125 ± 0.002	F814W	21.92 ± 0.1	3 × 10 <sup>−4</sup>	Gold	15
060801	14 <sup>h</sup> 12 <sup>m</sup> 01 <sup>s</sup> .262	+16°58′ 55″.97	1.131 ± 0.001	<i>r</i>	23.202 ± 0.11	0.02	Gold	8, 16
061006	07 <sup>h</sup> 24 <sup>m</sup> 07 <sup>s</sup> .808	−79°11′ 55″.188	0.461 ± 0.0007	<i>r</i>	24.153 ± 0.09	4 × 10 <sup>−4</sup>	Gold	2, 8, 17, This work
061201	...	...	...	F160W	≥26.4	...	Inconclusive	18
061210	09 <sup>h</sup> 38 <sup>m</sup> 05 <sup>s</sup> .362	+15°37′ 18″.877	0.4095 ± 0.0001	<i>r</i>	21.396 ± 0.05	0.02	Gold	8, 16
070429B	21 <sup>h</sup> 52 <sup>m</sup> 03 <sup>s</sup> .691	−38°49′ 42″.82	0.902 ± 0.001	<i>r</i>	23.283 ± 0.04	3 × 10 <sup>−3</sup>	Gold	8, 19
070707	17 <sup>h</sup> 50 <sup>m</sup> 58 <sup>s</sup> .555	−68°55′ 27″.60	...	F606W	26.857 ± 0.12	7.0 × 10 <sup>−3</sup>	Gold	18
070714B	03 <sup>h</sup> 51 <sup>m</sup> 22 <sup>s</sup> .272	+28°17′ 50″.943	0.923 ± 0.001	<i>r</i>	24.889 ± 0.21	5 × 10 <sup>−3</sup>	Gold	18–20
070724	01 <sup>h</sup> 51 <sup>m</sup> 14 <sup>s</sup> .068	−18°35′ 38″.47	0.457 ± 0.0007	<i>r</i>	20.776 ± 0.03	8 × 10 <sup>−4</sup>	Gold	8, 18, This work
070729	3 <sup>h</sup> 45 <sup>m</sup> 15 <sup>s</sup> .808	−39°19′ 18″.590	0.52 <sup>+1.17</sup> <sub>−0.28</sub>	<i>r</i>	23.019 ± 0.263	0.036	Silver	This work
070809	13 <sup>h</sup> 35 <sup>m</sup> 04 <sup>s</sup> .177	−22°08′ 33″.01	0.473	<i>r</i>	20.142 ± 0.02	6 × 10 <sup>−3</sup>	Gold	8, 18, 21
071227	3 <sup>h</sup> 52 <sup>m</sup> 31 <sup>s</sup> .026	−55°59′ 00″.89	0.381	<i>r</i>	20.635 ± 0.05	0.01	Gold	8, 17–18
080123	22 <sup>h</sup> 35 <sup>m</sup> 46 <sup>s</sup> .943	−64°53′ 54″.973	0.495	<i>r</i>	20.96 ± 0.05	0.11	Bronze	8
080503	19 <sup>h</sup> 06 <sup>m</sup> 28 <sup>s</sup> .901	+68°47′ 34″.78	...	F606W	27.151 ± 0.2	0.05	Silver	18, 22
080905A	19 <sup>h</sup> 10 <sup>m</sup> 42 <sup>s</sup> .045	−18°52′ 54″.51	0.1218 ± 0.0003	<i>R</i>	18.0 ± 0.5	0.01	Gold	18, 23
081226A	08 <sup>h</sup> 22 <sup>m</sup> 00 <sup>s</sup> .45	−69°01′ 49″.5	...	<i>r</i>	26.029 ± 0.34	0.01	Gold	24
090305A	16 <sup>h</sup> 07 <sup>m</sup> 07 <sup>s</sup> .596	−31°33′ 22″.54	...	F160W	25.292 ± 0.10	7 × 10 <sup>−3</sup>	Gold	18
090426A	12 <sup>h</sup> 36 <sup>m</sup> 18 <sup>s</sup> .047	+32°59′ 09″.46	2.609 <sup>b</sup>	F160W	25.57 ± 0.07	1.5 × 10 <sup>−4</sup>	Gold	18, 25
090510	22 <sup>h</sup> 14 <sup>m</sup> 12 <sup>s</sup> .623	−26°34′ 58″.55	0.903 ± 0.001	<i>i</i>	22.452 ± 0.14	8 × 10 <sup>−3</sup>	Gold	8, 18, 26
090515	10 <sup>h</sup> 56 <sup>m</sup> 35 <sup>s</sup> .847	+14°26′ 42″.84	0.403	<i>r</i>	20.268 ± 0.05	0.05	Silver	8, 18, 21
091109B	07 <sup>h</sup> 30 <sup>m</sup> 56 <sup>s</sup> .55	−54°05′ 23″.22	...	F110W	27.808 ± 0.24	0.11	Bronze	This work
100117A	00 <sup>h</sup> 45 <sup>m</sup> 04 <sup>s</sup> .661	−01°35′ 42″.02	0.914 ± 0.0004	<i>r</i>	24.40 ± 0.10	7 × 10 <sup>−5</sup>	Gold	18, 27
100206A	3 <sup>h</sup> 08 <sup>m</sup> 39 <sup>s</sup> .142	+13°09′ 29″.34	0.407 ± 0.002	<i>R</i>	21.53 ± 0.09	0.02	Gold	28, 29
100625A	1 <sup>h</sup> 03 <sup>m</sup> 10 <sup>s</sup> .918	−39°05′ 18″.44	0.452 ± 0.002	<i>r</i>	22.659 ± 0.09	0.04	Silver	30
101219A	4 <sup>h</sup> 58 <sup>m</sup> 20 <sup>s</sup> .497	−02°32′ 22″.45	0.7179 ± 0.0008	<i>r</i>	24.083 ± 0.05	0.06	Silver	30
101224A	19 <sup>h</sup> 03 <sup>m</sup> 41 <sup>s</sup> .919	45°42′ 48″.86	0.454 ± 0.0007	<i>r</i>	22.071 ± 0.052	0.015	Gold	This work
110112A	...	...	...	F110W	≥28.0	0.44	Inconclusive	This work
111117A	0 <sup>h</sup> 50 <sup>m</sup> 46 <sup>s</sup> .268	+23°00′ 41″.41	2.211 ± 0.001	<i>r</i>	23.789 ± 0.11	0.024	Silver	31–32
120305A	03 <sup>h</sup> 10 <sup>m</sup> 08 <sup>s</sup> .754	28°29′ 35″.87	0.225 ± 0.001	<i>r</i>	22.398 ± 0.050	0.053	Silver	This work
120804A	15 <sup>h</sup> 35 <sup>m</sup> 47 <sup>s</sup> .510	−28°46′ 56″.11	1.05 <sup>+0.23</sup> <sub>−0.09</sub>	<i>r</i>	26.406 ± 0.200	0.02	Gold	33, This work
121226A	11 <sup>h</sup> 14 <sup>m</sup> 34 <sup>s</sup> .121	−30°24′ 22″.84	1.37 <sup>+0.05</sup> <sub>−0.06</sub>	<i>r</i>	24.309 ± 0.06	0.019	Gold	This work
130515A	18 <sup>h</sup> 53 <sup>m</sup> 45 <sup>s</sup> .021	−54°16′ 50″.72	0.80 ± 0.01	<i>r</i>	22.651 ± 0.040	0.081	Silver	This work
130603B	11 <sup>h</sup> 28 <sup>m</sup> 48 <sup>s</sup> .231	+17°04′ 18″.61	0.3568 ± 0.0005	<i>r</i>	21.06 ± 0.06	2 × 10 <sup>−3</sup>	Gold	18, 34–35
130716A	11 <sup>h</sup> 58 <sup>m</sup> 17 <sup>s</sup> .862	+63°03′ 15″.35	2.2 <sup>+0.35</sup> <sub>−0.37</sub>	<i>r</i>	24.894 ± 0.344	0.36	Bronze	This work
130822A	1 <sup>h</sup> 51 <sup>m</sup> 42 <sup>s</sup> .708	−3°12′ 25″.447	0.154 ± 0.001	<i>r</i>	18.248 ± 0.063	0.086	Silver	This work
130912A	03 <sup>h</sup> 10 <sup>m</sup> 22 <sup>s</sup> .2	13°59′ 48″.74	...	F110W	27.471 ± 0.23	0.12	Bronze	This work
131004A	19 <sup>h</sup> 44 <sup>m</sup> 27 <sup>s</sup> .064	−2°57′ 30″.429	0.717 <sup>b</sup>	F110W	25.464 ± 0.09	0.055	Silver	36, This work
140129B	21 <sup>h</sup> 47 <sup>m</sup> 01 <sup>s</sup> .649	26°12′ 23″.270	0.43 ± 0.003	<i>r</i>	23.55 ± 0.07	8.7 × 10 <sup>−4</sup>	Gold	This work
140516A	...	...	...	<i>i</i>	≥26.1	...	Inconclusive	This work
				<i>K</i>	≥23.6	...		This work
140622A	21 <sup>h</sup> 08 <sup>m</sup> 41 <sup>s</sup> .744	−14°25′ 06″.166	0.959 ± 0.001	<i>r</i>	22.703 ± 0.042	0.10	Bronze	This work
140903A	15 <sup>h</sup> 52 <sup>m</sup> 03 <sup>s</sup> .265	+27°36′ 10″.71	0.3529 ± 0.0002	<i>r</i>	21.367 ± 0.194	6.2 × 10 <sup>−5</sup>	Gold	37, This work
140930B	0 <sup>h</sup> 25 <sup>m</sup> 23 <sup>s</sup> .473	+24°17′ 37″.93	1.465 ± 0.001	<i>r</i>	24.206 ± 0.248	0.021	Silver	This work
141212A	2 <sup>h</sup> 36 <sup>m</sup> 29 <sup>s</sup> .957	+18°08′ 47″.228	0.596 ± 0.001	<i>r</i>	22.945 ± 0.056	2.9 × 10 <sup>−4</sup>	Gold	This work
150101B	12 <sup>h</sup> 32 <sup>m</sup> 04 <sup>s</sup> .973	−10°56′ 00″.50	0.134 ± 0.003	<i>r</i>	16.604 ± 0.04	4.8 × 10 <sup>−4</sup>	Gold	38
150120A	0 <sup>h</sup> 41 <sup>m</sup> 16 <sup>s</sup> .563	+33°59′ 42″.598	0.4604 ± 0.0004	<i>r</i>	22.051 ± 0.063	1.9 × 10 <sup>−3</sup>	Gold	This work
150423A	...	...	1.394 <sup>b</sup>	F110W	≥28.1	...	Inconclusive	39, This work
150424A	10 <sup>h</sup> 09 <sup>m</sup> 13 <sup>s</sup> .406	−26°37′ 51″.745	...	F125W	26.293 ± 0.15	0.06	Bronze <sup>a</sup>	This work

**Table 2**  
(Continued)

GRB	R.A. (J2000)	Decl. (J2000)	Redshift	Filter	$m_{AB}$ (AB mag)	$P_{cc}$	Class	References
150728A	19 <sup>h</sup> 28 <sup>m</sup> 54 <sup>s</sup> .808	+33°54′ 58″22	0.461 ± 0.0005	<i>i</i>	21.420 ± 0.054	0.018	Gold	This work
150831A	14 <sup>h</sup> 44 <sup>m</sup> 05 <sup>s</sup> .939	−25°38′ 05″78	1.180 ± 0.001	<i>r</i>	24.434 ± 0.446	0.037	Silver	This work
151229A	21 <sup>h</sup> 57 <sup>m</sup> 28 <sup>s</sup> .701	−20°43′ 54″80	0.63 <sup>+0.49</sup> <sub>−0.35</sub>	<i>i</i>	24.924 ± 0.134	0.040	Silver	This work
160303A	11 <sup>h</sup> 14 <sup>m</sup> 48 <sup>s</sup> .119	+22°44′ 33″420	1.01 <sup>+0.18</sup> <sub>−0.23</sub>	F110W	23.774 ± 0.02	0.096	Silver	40, This work
160408A	8 <sup>h</sup> 10 <sup>m</sup> 29 <sup>s</sup> .580	+71°07′ 45″03	1.90 <sup>+0.38</sup> <sub>−0.53</sub>	<i>r</i>	25.736 ± 0.162	0.14	Bronze	This work
160410A	...	...	1.7177 ± 0.0001 <sup>b</sup>	<i>r</i>	>27.2	...	Inconclusive	41, This work
160411A	23 <sup>h</sup> 17 <sup>m</sup> 25 <sup>s</sup> .355	−40°14′ 30″56	0.82 <sup>+0.64</sup> <sub>−0.45</sub>	<i>r</i>	24.532 ± 0.134	7.2 × 10 <sup>−4</sup>	Gold	This work
160525B	9 <sup>h</sup> 57 <sup>m</sup> 32 <sup>s</sup> .246	+51°12′ 24″60	0.64 <sup>+2.03</sup> <sub>−0.14</sub>	<i>r</i>	23.29 ± 0.09	0.001	Gold	42, This work
160601A	15 <sup>h</sup> 39 <sup>m</sup> 43 <sup>s</sup> .949	+64°32′ 30″604	...	<i>z</i>	24.947 ± 0.344	8.9 × 10 <sup>−4</sup>	Gold	This work
160624A	22 <sup>h</sup> 00 <sup>m</sup> 46 <sup>s</sup> .145	+29°38′ 39″336	0.4842 ± 0.0005	<i>r</i>	21.960 ± 0.047	0.037	Silver	This work
160821B	18 <sup>h</sup> 39 <sup>m</sup> 53 <sup>s</sup> .994	+62°23′ 34″427	0.1619 ± 0.0002	<i>r</i>	19.548 ± 0.004	0.044	Silver	This work
160927A	...	...	...	<i>G</i>	≥25.7	...	Inconclusive	This work
				<i>J</i>	≥24.4	...		This work
161001A	4 <sup>h</sup> 47 <sup>m</sup> 40 <sup>s</sup> .530	−57°15′ 39″184	0.67 ± 0.02	<i>r</i>	22.968 ± 0.046	0.045	Silver	39, This work
161104A	05 <sup>h</sup> 11 <sup>m</sup> 34 <sup>s</sup> .37	−51°27′ 36″29	0.793 ± 0.003	<i>r</i>	23.847 ± 0.10	0.06	Bronze <sup>a</sup>	43
170127B	1 <sup>h</sup> 19 <sup>m</sup> 54 <sup>s</sup> .415	−30°21′ 29″615	2.28 ± 0.14	<i>r</i>	25.320 ± 0.290	0.098	Silver	This work
170428A	22 <sup>h</sup> 00 <sup>m</sup> 18 <sup>s</sup> .710	+26°54′ 56″280	0.453 ± 0.001	<i>r</i>	22.346 ± 0.100	6.7 × 10 <sup>−3</sup>	Gold	This work
170728A	3 <sup>h</sup> 55 <sup>m</sup> 33 <sup>s</sup> .116	+12°10′ 51″04	1.493 ± 0.009	<i>R</i>	24.735 ± 0.136	0.22	Bronze	This work
170728B	15 <sup>h</sup> 51 <sup>m</sup> 55 <sup>s</sup> .529	+70°07′ 22″038	1.272 ± 0.002	<i>r</i>	23.313 ± 0.096	8.3 × 10 <sup>−3</sup>	Gold	This work
180418A	11 <sup>h</sup> 20 <sup>m</sup> 29 <sup>s</sup> .21	24°55′ 58″734	1.56 <sup>+0.21</sup> <sub>−0.43</sub>	<i>r</i>	25.729 ± 0.21	1.5 × 10 <sup>−3</sup>	Gold	44, This work
180618A	11 <sup>h</sup> 19 <sup>m</sup> 45 <sup>s</sup> .801	+73°50′ 15″03	0.52 <sup>+0.09</sup> <sub>−0.11</sub>	<i>i</i>	22.183 ± 0.081	8.2 × 10 <sup>−3</sup>	Gold	This work
180727A	23 <sup>h</sup> 06 <sup>m</sup> 40 <sup>s</sup> .038	−63°03′ 07″088	1.95 <sup>+0.5</sup> <sub>−0.58</sub>	<i>r</i>	26.486 ± 0.277	8.6 × 10 <sup>−3</sup>	Gold	This work
180805B	1 <sup>h</sup> 43 <sup>m</sup> 07 <sup>s</sup> .655	−17°29′ 33″091	0.6612 ± 0.002	<i>r</i>	22.153 ± 0.063	0.042	Silver	This work
181123B	12 <sup>h</sup> 17 <sup>m</sup> 27 <sup>s</sup> .91	+14°35′ 52″27	1.754 ± 0.001	<i>r</i>	23.92 ± 0.19	4.4 × 10 <sup>−3</sup>	Gold	45
191031D	18 <sup>h</sup> 53 <sup>m</sup> 09 <sup>s</sup> .522	+47°38′ 40″13	1.93 <sup>+0.22</sup> <sub>−1.44</sub>	<i>r</i>	24.462 ± 0.263	0.043	Silver	This work
200219A	22 <sup>h</sup> 50 <sup>m</sup> 33 <sup>s</sup> .108	−59°07′ 11″579	0.48 ± 0.02	<i>r</i>	20.661 ± 0.05	2.2 × 10 <sup>−3</sup>	Gold	13, This work
200411A	03 <sup>h</sup> 10 <sup>m</sup> 39 <sup>s</sup> .135	−52°18′ 59″545	0.82 <sup>+0.18</sup> <sub>−0.17</sub>	<i>r</i>	22.564 ± 0.042	0.11	Bronze	13, This work
200522A	00 <sup>h</sup> 22 <sup>m</sup> 43 <sup>s</sup> .717	−00°16′ 57″466	0.5536 ± 0.0003	<i>r</i>	21.196 ± 0.02	3.5 × 10 <sup>−5</sup>	Gold	46–47
200907B	05 <sup>h</sup> 56 <sup>m</sup> 06 <sup>s</sup> .951	+6°54′ 22″637	0.56 <sup>+1.39</sup> <sub>−0.32</sub>	<i>i</i>	23.936 ± 0.108	9 × 10 <sup>−3</sup>	Gold	This work
201006A <sup>d</sup>	...	...	...	<i>K</i>	≥23.6	...	Constraint	This work
201221D	11 <sup>h</sup> 24 <sup>m</sup> 14 <sup>s</sup> .064	+42°08′ 40″047	1.055 ± 0.001	<i>r</i>	23.418 ± 0.076	0.12	Bronze	48, This work
210323A	21 <sup>h</sup> 11 <sup>m</sup> 47 <sup>s</sup> .320	+25°22′ 09″989	0.733 ± 0.001	<i>r</i>	24.972 ± 0.252	0.013	Gold	This work
210726A	12 <sup>h</sup> 53 <sup>m</sup> 09 <sup>s</sup> .820	+19°11′ 25″032	0.37 <sup>+0.32</sup> <sub>−0.17</sub>	<i>i</i>	25.211 ± 0.289	7.3 × 10 <sup>−5</sup>	Gold	13, This work
210919A	05 <sup>h</sup> 21 <sup>m</sup> 01 <sup>s</sup> .954	+1°18′ 40″022	0.2415 ± 0.001	<i>r</i>	20.50 ± 0.05	0.13	Bronze	13, This work
211023B	11 <sup>h</sup> 21 <sup>m</sup> 14 <sup>s</sup> .311	+39°08′ 08″36	0.862 ± 0.001	<i>r</i>	24.361 ± 0.377	4.7 × 10 <sup>−3</sup>	Gold	13, This work
211106A	22 <sup>h</sup> 54 <sup>m</sup> 20 <sup>s</sup> .541	−53°13′ 50″548	...	F814W	25.791 ± 0.069	5.5 × 10 <sup>−4</sup>	Gold	This work, 49
211211A <sup>c</sup>	14 <sup>h</sup> 09 <sup>m</sup> 10 <sup>s</sup> .467	+27°53′ 21″050	0.0763 ± 0.0002	F606W	19.57 ± 0.01	0.0136	Gold	50
170817A <sup>e</sup>	13 <sup>h</sup> 09 <sup>m</sup> 47 <sup>s</sup> .70	−23°23′ 02″0	0.009787 ± 0.000057	<i>r</i>	12.44 ± 0.01	4.9 × 10 <sup>−4</sup>	...	51–52

**Notes.** Magnitudes  $m_{\lambda}$  are not corrected for Galactic extinction,  $A_{\lambda}$ , in the direction of the burst. Photometric redshift uncertainties correspond to 68% confidence and the methods to determine them are described in Nugent et al. (2022).

<sup>a</sup> Hosts reclassified as Bronze due to at least one other galaxy with comparably low  $P_{cc}$  value in the field.

<sup>b</sup> Redshift determined from afterglow.

<sup>c</sup> Long-duration GRBs thought to be associated with NS merger origins.

<sup>d</sup> This burst has a high Galactic extinction of  $A_V = 3.5$  mag and is therefore considered an observing constraint burst with a sightline that precludes a meaningful host galaxy search in the optical bands. However, we report a *K*-band limit here on a galaxy within the XRT position for completeness.

<sup>e</sup> This host is only considered as a point of comparison to the cosmological short GRB sample.

**References.** (1) Bloom et al. (2006), (2) Fong et al. (2010), (3) Albareti et al. (2017), (4) Skrutskie et al. (2006), (5) Covino et al. (2006), (6) Fox et al. (2005), (7) Hjorth et al. (2005), (8) Leibler & Berger (2010), (9) Berger et al. (2005), (10) Gorosabel et al. (2006), (11) Ferrero et al. (2007), (12) Prochaska et al. (2006), (13) Schlegel et al. (2021), (14) Soderberg et al. (2006), (15) Gal-Yam et al. (2006), (16) Berger et al. (2007), (17) D’Avanzo et al. (2009), (18) Fong & Berger (2013), (19) Cenko et al. (2008), (20) Graham et al. (2009), (21) Berger (2010), (22) Perley et al. (2009), (23) Rowlinson et al. (2010), (24) Nicuesa Guelbenzu et al. (2012), (25) Levesque et al. (2010), (26) McBreen et al. (2010), (27) Fong et al. (2011), (28) Perley et al. (2012), (29) Wright et al. (2010), (30) Fong et al. (2013), (31) Margutti et al. (2012), (32) Selsing et al. (2018), (33) Berger et al. (2013), (34) de Ugarte Postigo et al. (2014), (35) Cucchiara et al. (2013), (36) Chornock et al. (2013), (37) Troja et al. (2016), (38) Fong et al. (2016), (39) Selsing et al. (2019), (40) Cano et al. (2016), (41) Agüí Fernández et al. (2021), (42) O’Connor et al. (2022), (43) Nugent et al. (2020), (44) Rouco Escorial et al. (2021), (45) Paterson et al. (2020), (46) Chambers et al. (2016), (47) Fong et al. (2021), (48) Kilpatrick et al. (2020), (49) Laskar et al. (2022), (50) Rastinejad et al. (2022), (51) Blanchard et al. (2017), (52) Wenger et al. (2000).

(This table is available in machine-readable form.)

counts from galaxy surveys (compiled in Hogg et al. 1997; Beckwith et al. 2006 and Metcalfe et al. 2006) and integrate the relevant function for  $m \leq m_i$  depending on the filter of the observation. For the value of  $R_i$ , we use the maximum of  $\delta R$  or  $\sigma_{\text{GRB}}$ , which is an approximation of the methods described in Bloom et al. (2002) and Blanchard et al. (2016), in the absence of effective radii measurements for all putative GRB hosts. If the most proximal extended source has  $P_{\text{cc}} \lesssim 0.01$ , we consider it to be the host galaxy of that burst.

If the most proximal source to the GRB has  $P_{\text{cc}} \gtrsim 0.01$ , we continue to perform photometry of all extended sources in the image using the IRAF/apphot package. We discard noticeably fainter galaxies with increasing angular distance  $\delta R$  from the burst since these objects will have a lower probability of being the host galaxy based on chance alignment arguments. We then calculate  $P_{\text{cc}}$  for each of these sources. For each burst, the minimum in the probability function,  $P_{\text{cc},\text{min}}$ , corresponds to the most probable host galaxy. In many cases, this still ends up being the most proximal host galaxy, although in some cases a galaxy at a larger separation is favored as the host.

#### 4.3. Gold, Silver, and Bronze Samples

In general, the  $P_{\text{cc}}$  method can recover clear host galaxies for most bursts. However, it favors apparently brighter galaxies at a given angular separation, and it is difficult to interpret if two putative hosts for a given burst have similarly low  $P_{\text{cc}}$  values. To reflect the varying robustness of associations and the nuances of the method, we divide our sample into four categories based on the minimum probability of chance coincidence value,  $P_{\text{cc},\text{min}}$  as follows:

1. *Gold*: Bursts with putative hosts that have  $P_{\text{cc},\text{min}} \leq 0.02$ . There are 50 events in the Gold sample. These represent short GRBs with the most robust host associations, although they are likely to be biased toward bursts with subarcsecond localizations (e.g., optical afterglows), smaller offsets, and apparently brighter hosts.
2. *Silver*: Bursts with putative hosts that have  $0.02 < P_{\text{cc},\text{min}} \leq 0.10$ . There are 21 events in the Silver sample. These represent short GRBs with moderately robust host associations. This sample is subject to less of the biases outlined for the Gold sample.
3. *Bronze*: Bursts with putative hosts that have  $0.10 < P_{\text{cc},\text{min}} \leq 0.20$ . There are 13 events in the Bronze sample. These represent short GRBs with the least robust host associations, but for which more probable alternatives do not exist. There is likely a small loss of integrity in individual host assignments (addressed in Section 7). However, this is an important sample to include as it is least subject to the biases of the  $P_{\text{cc}}$  assignment method.
4. *Inconclusive*: Bursts for which the lowest value for an extended source in the field is  $P_{\text{cc},\text{min}} > 0.20$ . There are six events in the Inconclusive sample. In all cases, there are deep optical or NIR limits on a coincident host galaxy to  $\gtrsim 26$ –28 mag.

In general, we follow the above guidelines to associate each short GRB with its host galaxy. However, we make three exceptions and modifications to the above scheme based on information from their afterglows, or an analysis that yields multiple putative hosts with similarly low  $P_{\text{cc}}$  values.

For GRB 150424A, the first and second closest galaxies (in angular separation) have similar values of  $P_{\text{cc}} = 0.06$  and  $0.04$ , respectively, both of which would place the burst in the Silver sample. The second closest galaxy has a spectroscopic redshift of  $z = 0.3$ , but this is at odds with the inferred value from the afterglow SED, which implies  $z = 1.0^{+0.3}_{-0.2}$  (Castro-Tirado et al. 2015; Knust et al. 2017). Instead, the closest galaxy, which was first reported in early HST imaging (Tanvir et al. 2015), has a probable redshift range of  $z \approx 0.9$ –1.6 based on the likely location of the 4000 Å break (Jin et al. 2018). Thus, despite having a slightly higher  $P_{\text{cc}}$  value, we conclude that the closest galaxy is the most likely host of GRB 150424A. We downgrade this burst to the Bronze sample given the more ambiguous nature of this association.

For GRB 161104A, the galaxies with the two lowest  $P_{\text{cc}}$  values have  $P_{\text{cc}} = 0.06$  and  $0.08$  (Nugent et al. 2020), which would nominally place this burst in the Silver sample. The closest galaxy, with  $P_{\text{cc}} = 0.06$ , is fully encompassed in the XRT position and is part of a galaxy cluster at  $z \approx 0.79$ . We consider this to be the host galaxy, but we also demote this burst to the Bronze sample.

Finally, for GRB 061201, there are two galaxies at very different offsets that have identical  $P_{\text{cc}}$  values of  $0.07$ , which would be a Silver sample burst. While one of the putative hosts is at  $z = 0.111$  and has previously been considered as a tentative association (Stratta et al. 2007; Fong & Berger 2013), we cannot conclude on an individual host association and consider this to be an Inconclusive burst.

Overall, we make associations for 84 events. The resulting minimum  $P_{\text{cc}}$  value, corresponding to the most probable host galaxy, for each short GRB is listed in Table 2. We also list the optical or NIR magnitude, and the host classification (Gold, Silver, Bronze, Inconclusive). We confirm many associations that were previously made in the literature, as well as make 26 new identifications.<sup>29</sup> We also revise associations for three bursts: GRBs 070729, 161001A, and 191031D. For GRB 070729, the XRT position shifted significantly compared to the initial published position on which the host association was made. The updated position coincides with a faint source on the edge of the XRT position (90% confidence) while the original host published in Leibler & Berger (2010) now has a substantially larger value of  $P_{\text{cc}}$ . For GRB 161001A, Selsing et al. (2019) note a faint extended source in the wings of an M star that overlaps with the XRT position with  $z = 0.891$ , which is taken to be the host galaxy. However, this galaxy is not apparent in our imaging and instead we find a (presumably) brighter  $r \approx 22.9$  mag galaxy coincident with the XRT position (Figure 2). We consider this to be the host galaxy and determine a photometric redshift of  $z \approx 0.67$ . Finally, for GRB 191031D, O’Connor et al. (2022) identified a galaxy outside of the XRT position at  $z \approx 0.5$  as the host. However, our deep Keck NIR imaging reveals a red, extended source within the XRT position with  $P_{\text{cc}} = 0.04$  (compared to the larger value of  $P_{\text{cc}} \approx 0.1$  for the galaxy identified by O’Connor et al. 2022). Thus, we revise this host identification and photometric redshift to  $z \approx 1.9$ . We use the categories in our downstream analysis and in Nugent et al. (2022).

<sup>29</sup> In addition, we corroborate the host associations of eight short GRBs recently reported in O’Connor et al. (2022).

#### 4.4. Inconclusive Host Associations

We show the fields of the six bursts in the Inconclusive host association class in Figure 3. We also show a seventh burst, GRB 201006A, which has a high-extinction sightline through the galaxy of  $A_V = 3.5$  mag but for which we have deep  $K$ -band imaging in which the extinction is less severe. Thus, we consider this burst to have meaningful information at NIR wavelengths only. Five have subarcsecond localizations from optical afterglows while two (GRBs 140516A and 201006A) only have XRT positions.

This class of bursts was formerly termed *host-less* (Berger 2010). The fields of GRBs 061201, 110112A, and 160410A were previously studied and classified as such (Berger 2010; Fong & Berger 2013; Agüí Fernández et al. 2021) (although deeper HST imaging for GRB 110112A is presented here). We introduce four new cases. Both GRB 140516A<sup>30</sup> and 201006A have faint extended sources in the vicinity of their XRT positions (90% confidence) although no galaxy reaches the threshold of  $P_{cc,min} \leq 0.2$ .

Two of these bursts, GRBs 150423A and 160410A, have known redshifts from their afterglows (Selsing et al. 2019; Agüí Fernández et al. 2021; Table 2). From HST imaging, we find that GRB 150423A has no host to  $m_{F110W} \gtrsim 28.1$  mag at the position of its optical afterglow, constraining any spatially coincident galaxy to  $L_r \lesssim 3 \times 10^8 L_\odot$  at  $z = 1.394$ . The most probable host galaxy using the  $P_{cc}$  method has  $z = 0.456$  (Perley 2015) with  $P_{cc} \approx 0.2$ , but is inconsistent with the afterglow redshift. Meanwhile, the next most probable host galaxy (and the one at the smallest angular separation to the afterglow) has  $P_{cc} = 0.23$ , too high to meet the Bronze class threshold. For GRB 160410A at  $z = 1.7177$ , the reported limit is  $r \gtrsim 27.2$  mag (Agüí Fernández et al. 2021), which constrains any coincident host to  $L_r \lesssim 1.6 \times 10^9 L_\odot$ .

Overall, while this population may represent bursts with the largest offsets, and is thus an important population to include, it comprises only a small fraction of the total short GRBs in this sample. We also note that several formerly host-less bursts have associations that meet the threshold to fall in one of the Gold, Silver, or Bronze categories, thus highlighting the importance of using a uniform method across all bursts for association.

### 5. Spectroscopic Catalog and Data Analysis

The second major goal of this study is to build a spectroscopic catalog of short GRB host galaxies. We draw from new spectroscopic observations, archival data that were previously published in the literature, and donated reduced spectra from corresponding authors.

#### 5.1. Spectroscopic Observations

We obtained spectroscopic observations for 22 short GRB hosts with unpublished spectra: GRBs 101224A, 120305A, 130822A, 140129B, 140622A, 140930B, 141212A, 150120A, 150728A, 150831A, 151229A, 161001A, 160411A, 170428A, 170728A, 170728B, 180618A, 180805B, 201221D, 210323A, 210919A, and 211023B. For these observations, we used the twin 6.5 m Magellan/Baade and Clay telescopes, 8 m Gemini-North and Gemini-South telescopes, 6.5 m MMT, twin 10 m

Keck I and II telescopes, and the twin 8.4 m LBT. Additionally, we obtained our own spectroscopic observations for four short GRBs which have previously published spectra from other telescopes and have known redshifts: GRBs 070724A (Leibler & Berger 2010), 140903A (Troja et al. 2016), 160624A (O'Connor et al. 2021), and 160821B (Kasliwal et al. 2017). We list the telescope and instruments used for these new observations in Table 1, as well as the details of the spectra in Table 3.

We also draw from archival and literature sources to obtain spectroscopy for the remaining host galaxies. Our aim is to build as complete a spectroscopic catalog as possible to enable the uniform stellar population modeling analysis in Nugent et al. (2022). Thus, we first retrieved the raw 2D spectra and calibration files of 10 short GRB hosts from observatory archives for re-reduction and analysis. We note that these same spectra were previously published in the following works: GRBs 050509B (Bloom et al. 2006), 050709 (Fox et al. 2005), 050724 (Berger et al. 2005), 051221A (Soderberg et al. 2006), 060614 (Niino et al. 2017), 060801 (Berger et al. 2007), 061006 (Berger et al. 2007), 070429B (Cenko et al. 2008), 070714B (Cenko et al. 2008), and 090510 (McBreen et al. 2010). From the literature, we also obtained reduced 1D object and error spectra for 10 events from the corresponding authors: GRBs 100117A (Fong et al. 2011), 100206A (Perley et al. 2012), 100625A, 101219A (Fong et al. 2013), 130603B (Cucchiara et al. 2013), 150101B (Fong et al. 2016), 161104A (Nugent et al. 2020), 181123B (Paterson et al. 2020), 200522A (Fong et al. 2021), and 211211A (Rastinejad et al. 2022). This archival and literature sample uses Magellan, Gemini, Keck, and the VLT. We list the details of these spectra, when available, in Table 3.

#### 5.2. Spectroscopic Reduction and Analysis

We use a combination of reduction tasks and methods depending on the origin of the spectra. For the subset of 10 host galaxies with spectra taken with LBT/MODS, Magellan (IMACS and LDSS), and Keck/LRIS (GRBs 101224A, 120305A, 130515A, 130822A, 140622A, 140903A, 140930B, 160411A, 160624A, and 201221D), we use standard IRAF tasks in the `ccdred`, `longslit`, and `immatch` packages to process and co-add the data (Tody 1986, 1993). For each set of data, we subtract the overscan regions or apply bias corrections, apply flat-field corrections, model the sky background, and subtract this background from the individual frames. We co-add individual background-subtracted 2D frames and then use IRAF/`apall` to extract the 1D spectra. We perform wavelength calibration using standard arc lamp spectra (HgNeArKrXe for MODS, HeNeAr for LDSS, NeArKrXe for IMACS, and HgNeArCdZn for LRIS). We apply spectrophotometric flux calibration using standard stars taken at a similar airmass on the same night in the same spectral setup as the host spectra. We determine the error spectrum by performing the aforementioned reduction steps, but on the 2D spectra without sky subtraction. We perform standard error propagation in the combination. The spectra for six of these short GRB hosts are shown in Figure 4.

For five hosts (GRBs 050709, 050724, 051221A, 060801, and 061006) with Gemini/GMOS (EEV detector) observations, we use the `gemini/gmos` IRAF package. We apply bias subtraction, flat-field corrections, and model the sky background. We determine the wavelength solutions using CuAr arc lamps and calibrate the individual 2D science frames

<sup>30</sup> We note that the brighter object on the outskirts of the XRT position is a star.

**Table 3**  
Log of Spectroscopic Observations

GRB	Facility/Instrument	Exposures	Lines Identified	Previously Published?	Re-reduced?	Reduction Method
050509B	Keck/DEIMOS	3 × 300	Ca II H&K	Bloom et al. (2006)	Yes	PypeIt
050709	Gemini/GMOS	2 × 1200	H $\beta$ , [O III] $\lambda\lambda$ 4959, 5007	Fox et al. (2005)	Yes	IRAF
050724	Gemini/GMOS	4 × 1800	Ca II H&K	Berger et al. (2005)	Yes	IRAF
051221A	Gemini/GMOS	2 × 1800	[O II] $\lambda$ 3727, H $\beta$ , [O III] $\lambda\lambda$ 4959, 5007	Soderberg et al. (2006)	Yes	IRAF
060614	Gemini/GMOS	4 × 1200	[O III] $\lambda\lambda$ 4959, 5007, H $\alpha$	Niino et al. (2017)	Yes	PypeIt
060801	Gemini/GMOS	2 × 900	[O II] $\lambda$ 3727	Berger et al. (2007)	Yes	IRAF
061006	Gemini/GMOS	2 × 1830	[O II] $\lambda$ 3727, [O III] $\lambda\lambda$ 4959, 5007	Berger et al. (2007)	Yes	IRAF
070429B	Keck/LRIS	2 × 1500	[O II] $\lambda$ 3727	Cenko et al. (2008)	Yes	PypeIt
070714B	Keck/LRIS	1 × 2100	[O II] $\lambda$ 3727	Cenko et al. (2008)	Yes	PypeIt
070724A <sup>a</sup>	Keck/DEIMOS	2 × 1800	[O II] $\lambda$ 3727, [Ca II]H&K, H $\beta$ , [O III] $\lambda\lambda$ 4959, 5007	No	Yes	PypeIt
090510	VLT/FORS2	1 × 1800	[O II] $\lambda$ 3727, [O III] $\lambda$ 5007	McBreen et al. (2010)	Yes	PypeIt
100117A	Gemini/GMOS	4 × 1460	Ca II H&K	Fong et al. (2011)	No	...
100206A	Keck/LRIS	2 × 600	[O II] $\lambda$ 3727, Ca II H&K, H $\beta$ , [O III] $\lambda\lambda$ 4959, 5007, H $\alpha$ , [N II] $\lambda\lambda$ 6549, 6584, [S II] $\lambda\lambda$ 6717, 6731	Perley et al. (2012)	No	...
100625A	Magellan/LDSS	2 × 2700	Ca II H&K, H $\beta$ , H $\delta$	Fong et al. (2013)	No	...
101219A	Gemini/GMOS	4 × 1800	[O II] $\lambda$ 3727, H $\beta$ , [O III] $\lambda\lambda$ 4959, 5007	Fong et al. (2013)	No	...
101224A	LBT/MODS	8 × 600	H $\gamma$ , H $\beta$ , [O III] $\lambda\lambda$ 4959, 5007, H $\alpha$	No	Yes	IRAF
120305A	LBT/MODS	2 × 900	[O III] $\lambda$ 5007, H $\alpha$	No	Yes	IRAF
130515A	Magellan/IMACS	2 × 1200	None	No	Yes	IRAF
130603B	Gemini/GMOS	2 × 900	[O II] $\lambda$ 3727, H $\beta$ , [O III] $\lambda\lambda$ 4959, 5007	Cucchiara et al. (2013)	No	...
130822A	LBT/MODS	3 × 600	[O II] $\lambda$ 3727, H $\beta$ , H $\alpha$	No	Yes	IRAF
140129B	Keck/DEIMOS	3 × 1800	[O II] $\lambda$ 3727, H $\beta$ , [O III] $\lambda$ 5007	No	Yes	PypeIt
140622A	Magellan/LDSS	2 × 1800	[O II] $\lambda$ 3727, H $\beta$	No	Yes	IRAF
140903A <sup>a</sup>	Keck/LRIS	2 × 1200	[O III] $\lambda$ 5007, H $\alpha$	No	Yes	IRAF
140930B	LBT/MODS	4 × 1200	[O II] $\lambda$ 3727	No	Yes	IRAF
141212A	Gemini/GMOS	3 × 900	H $\beta$ , [O III] $\lambda\lambda$ 4959, 5007	No	Yes	PypeIt
150101B	Magellan/IMACS	2 × 600	H $\beta$ , Mg $\lambda$ 5175, NaD $\lambda$ 5892, TiO $\lambda$ 7050	Fong et al. (2016)	No	...
150120A	Gemini/GMOS	1 × 900	[O II] $\lambda$ 3727, H $\beta$	No	Yes	PypeIt
150728A	Keck/DEIMOS	3 × 1800	[O II] $\lambda$ 3727, H $\beta$ , [O III] $\lambda\lambda$ 4959, 5007	No	Yes	PypeIt
150831A	Keck/LRIS	3 × 1200	[O II] $\lambda$ 3727	No	No	PypeIt
151229A	Keck/LRIS	3 × 1200	None	No	Yes	PypeIt
160411A	Magellan/LDSS	3 × 1800	None	No	Yes	IRAF
160624A <sup>a</sup>	LBT/MODS	8 × 600	H $\beta$ , [O III] $\lambda$ 5007	No	Yes	IRAF
160821B <sup>a</sup>	Keck/DEIMOS	2 × 900	H $\gamma$ , H $\beta$ , [O III] $\lambda\lambda$ 4959, 5007	No	Yes	PypeIt
161104A	Magellan/IMACS	3 × 1800	Ca II H&K	Nugent et al. (2020)	No	...
170428A	MMT/Binospec	4 × 900	[O II] $\lambda$ 3727, [O III] $\lambda$ 5007	No	Yes	MMT/IRAF
170728A	Keck/DEIMOS	3 × 1800	[O II] $\lambda$ 3727	No	Yes	PypeIt
170728B	MMT/Binospec	6 × 900	[O II] $\lambda$ 3727	No	No	MMT/IRAF
180805B	Keck/LRIS	2 × 1200	[O II] $\lambda$ 3727, H $\gamma$ , H $\beta$ , [O III] $\lambda\lambda$ 4959, 5007	No	Yes	PypeIt
180618A	MMT/Binospec	2 × 1800	None	No	Yes	MMT/IRAF
181123B	Gemini/FLAMINGOS	30 × 120	H $\beta$	Paterson et al. (2020)	No	...
200522A	Keck/LRIS	3 × 900	[O II] $\lambda$ 3727, H $\gamma$ , H $\beta$ , [O III] $\lambda\lambda$ 4959, 5007	Fong et al. (2021)	No	...
201221D	Keck/LRIS	3 × 1240	[O II] $\lambda$ 3727	No	Yes	IRAF
210323A	Keck/DEIMOS	3 × 1800	[O II] $\lambda$ 3727, [O III] $\lambda\lambda$ 4959, 5007	No	Yes	PypeIt
210919A	Keck/DEIMOS	3 × 1800	[O II] $\lambda$ 3727, [O III] $\lambda$ 4959, [O III] $\lambda$ , H $\alpha$	No	Yes	PypeIt
211023B	Keck/DEIMOS	2 × 1800	[O II] $\lambda$ 3727, [O III] $\lambda\lambda$ 4959, 5007	No	Yes	PypeIt
211211A	Keck/DEIMOS	2 × 1500	H $\beta$ , [O III] $\lambda\lambda$ 4959, 5007, H $\alpha$ , [N II] $\lambda\lambda$ 6549, 6584, [S II] $\lambda\lambda$ 6717, 6731	Rastinejad et al. (2022)	No	...

**Note.** Spectroscopic observations of short GRB host galaxies. Reduction methods are stated for bursts analyzed or re-analyzed in this work. Spectra that were not re-reduced were donated by the corresponding authors to this work for the BRIGHT database.

<sup>a</sup> These hosts have different previously published spectra than the ones presented here. Our new spectra taken with different instruments of the same objects are consistent with the literature findings (GRBs 070724A: Berger et al. 2009; 140903A: Troja et al. 2016, 160624A: O'Connor et al. 2021, and 160821B: Lamb et al. 2019a).

with the `gswavelength` and `gssubtract` tasks. We apply flux calibration to the spectra with a standard star taken within the same observing semester. We extract the 1D spectra with `gsextract` and combine these with `gscombine`. The Gemini IRAF package propagates variance in traces through each task, which we use to determine the final error spectra.

For three hosts (GRB 170428A, 170728B, and 180618A), we obtain 1D, co-added, flux and wavelength-calibrated spectra from the MMT/Binospec observatory products. This data was reduced with the instrument's spectroscopic reduction software, which is based on IDL.<sup>31</sup> The software automatically applies a flat-field and sky background correction. It uses a barycentric wavelength calibration and flux calibrates based on the spectrophotometric standard taken on the same night at a similar airmass. It extracts a 1D spectrum from co-added 2D frames, using a 1'' radius, and provides an uncertainty, which we use as the error spectrum.

Finally, for 19 hosts with data from Keck (DEIMOS and LRIS), Gemini/GMOS (E2V and Hamamatsu detectors), and VLT/FORS2, we used the Python Spectroscopic Data Reduction Pipeline (`PyPeIt`; Prochaska et al. 2020) for data processing and spectral extraction. These hosts are GRBs 050509B, 060614, 070429B, 070714B, 070724A, 090510, 140129B, 141212A, 150120A, 150728A, 150831A, 151229A, 160821B, 170728A, 180805B, 191031D, 210323A, 210919A, and 211023B (Table 3). In `PyPeIt`, we apply an overscan and/or bias subtraction, flat-field correction and perform wavelength calibration and spectral extraction (using the `boxcar` method with a 1.5–2.5 radius, in order to include all of the emission line flux). We apply flux calibrations using appropriate spectrophotometric standards. We co-add the flux-calibrated 1D spectra and apply a telluric correction using an atmospheric model. `PyPeIt` determines the variance on each trace, which we use to determine the error spectra.

For all 26 new and unpublished spectra in our sample as well as the 10 re-reduced spectra, we use the Cardelli et al. (1989) extinction law and the  $A_V$  in the direction of each burst (Schlafly & Finkbeiner 2011) to correct for Galactic extinction. We then normalize the host spectra to their extinction-corrected photometry. The final 1D spectra of 18 hosts with determined redshifts and their spectral line identifications are displayed in Figure 4. Not shown are the four new spectra which have consistent results with previous works.

### 5.3. Feature Identification and Redshift Determinations

For 22 hosts of the 24 hosts with new, unpublished spectroscopic observations, we determine redshifts through feature identification. The most common features in our spectra are [O II] $\lambda$ 3727, H $\beta$ , [O III] $\lambda$ 4959, [O III] $\lambda$ 5007, and H $\alpha$  for star-forming galaxies, and the Ca II H&K for quiescent or transitioning galaxies. We search for high S/N spectral lines (S/N > 5) with Gaussian-like structures in both the 1D and 2D frames. When multiple spectral lines are found, we use the mean of the Gaussian lines to determine ratios between each pair of lines. We compare these ratios to those of the rest-frame wavelengths of spectral lines at redshifts between  $0 \leq z \leq 3.0$ . We require that the ratios of observed lines are within 0.1% of the rest-frame spectral line ratios to maintain accuracy in line determination. From there, we can determine what each observed line is and the redshift. We determine error on the

redshift by fitting the spectral lines and their direct background ( $\sim \pm 100$  Å) with a Gaussian profile and determining the mean of  $1\sigma$  uncertainties on each line.

For 16 hosts, we have at least two spectral lines with S/N > 5 above the continuum from which we can determine a common redshift. Out of these 16, 6 are completely new redshifts, unconfirmed in GCNs or other works. The redshifts of GRBs 101224A, 130822A, 140622A, 170428A, and 180805B are consistent with those reported in O'Connor et al. (2022). A few redshifts were reported in GCNs and are also consistent with our findings: GRBs 141212A (Chornock et al. 2014) and 210919A (Rossi et al. 2022). The GCN redshift of 211023B (Rossi et al. 2021) is slightly inconsistent with our result and only based on one detected emission line; thus we consider this a new redshift.

For five hosts (GRBs 140930B, 150831A,<sup>32</sup> 170728A, 170728B, 201221D), we can only identify a single emission line. However, in all cases the width of this line is double-peaked in nature, suggesting it is likely a doublet, specifically the [O II] $\lambda$ 3727, 3729 doublet. In addition, these lines were all found at higher wavelengths (>9100 Å for GRBs 140930B and 170728A, >8100 Å for GRBs 150831A and 170728B, and  $\approx 7659$  Å for GRB 201221D). If these lines were instead H $\beta$  or [O III], we would expect to detect the [O II], H $\beta$ , and [O III] in all five spectra, or if these lines were H $\alpha$ , we would be able to detect all the common emission lines in the spectra of GRBs 140930B, 150831A, 170728B, and 201221D, and everything but [O II] in the spectrum of 170728A. Given that these additional lines are not detected, despite the wavelength coverage of these spectra, it is most likely that the identified lines are [O II]. Therefore, in all three cases, we identify the line as the [O II] $\lambda$ 3727 doublet. GRBs 140930B, 150831A, 170728A, and 170728B do not have published spectroscopy or redshifts so we report these redshifts for the first time. Our redshift of  $z = 1.055 \pm 0.001$  is close, although not formally consistent with, the previously reported redshift in the GCNs ( $z = 1.045$ ; de Ugarte Postigo et al. 2020). We present all spectroscopic redshifts and uncertainties in Table 2.

For short GRBs with photometric data only, we use the stellar population inference code `Prospector` (Leja et al. 2017; Johnson et al. 2021) to model their SEDs and determine their photometric redshifts. The full stellar population modeling methods and analysis are described in Nugent et al. (2022, Appendix for fits). We note that our photometric redshifts for five GRBs (070729, 120804A, 151229A, 191031D, and 200411A) differ from the literature, due to a combination of modeling assumptions (such as truncated redshift priors in other works), less complete data sets, or incorrect host associations. Combined with the literature sample, we find a median redshift for the full population of 0.64 with a 68% credible interval on the distribution of  $[-0.32, +0.83]$ , and a higher median and credible interval of 0.93  $[-0.46, +1.16]$  for the photometric redshift population; this is discussed and explored in more detail in Nugent et al. (2022).

<sup>32</sup> We find a tentative detection of a low S/N emission line at  $\approx 8124$  Å. Were this line real and [O II], the redshift would fall within the expected `Prospector` photometric redshift range of  $z = 1.09^{+0.10}_{-0.19}$ . There is also significant evidence for a 4000 Å break in the photometric continuum within this redshift range, as well.

<sup>31</sup> [https://bitbucket.org/chil\\_sai/binospec/wiki/Home](https://bitbucket.org/chil_sai/binospec/wiki/Home)

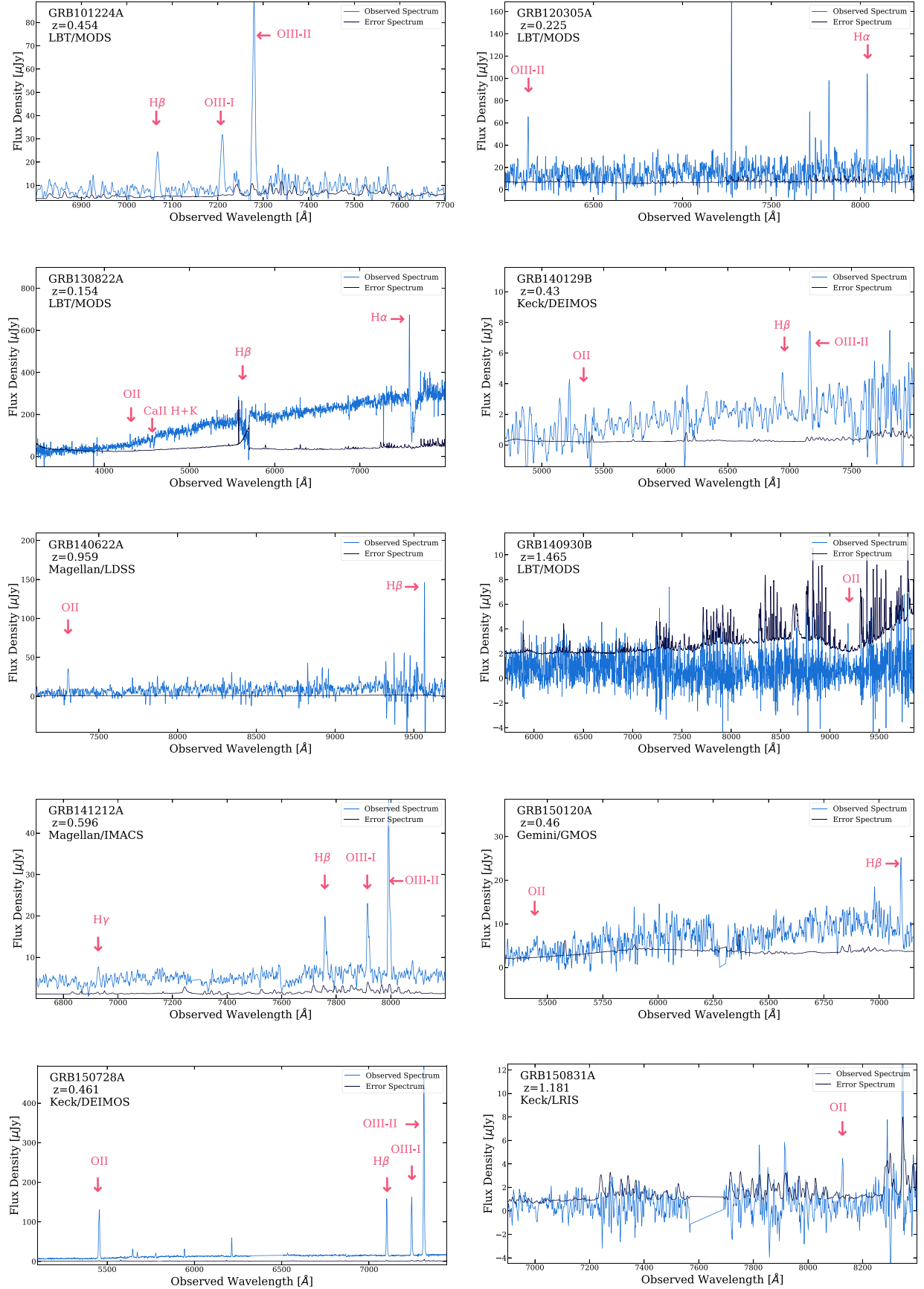


**Figure 4.** Optical spectroscopy of 18 short GRB host galaxies that are newly presented in this work. In each panel, the spectral lines which enable redshift determination are denoted. Four additional new spectra have consistent results with previous works and thus are not shown.

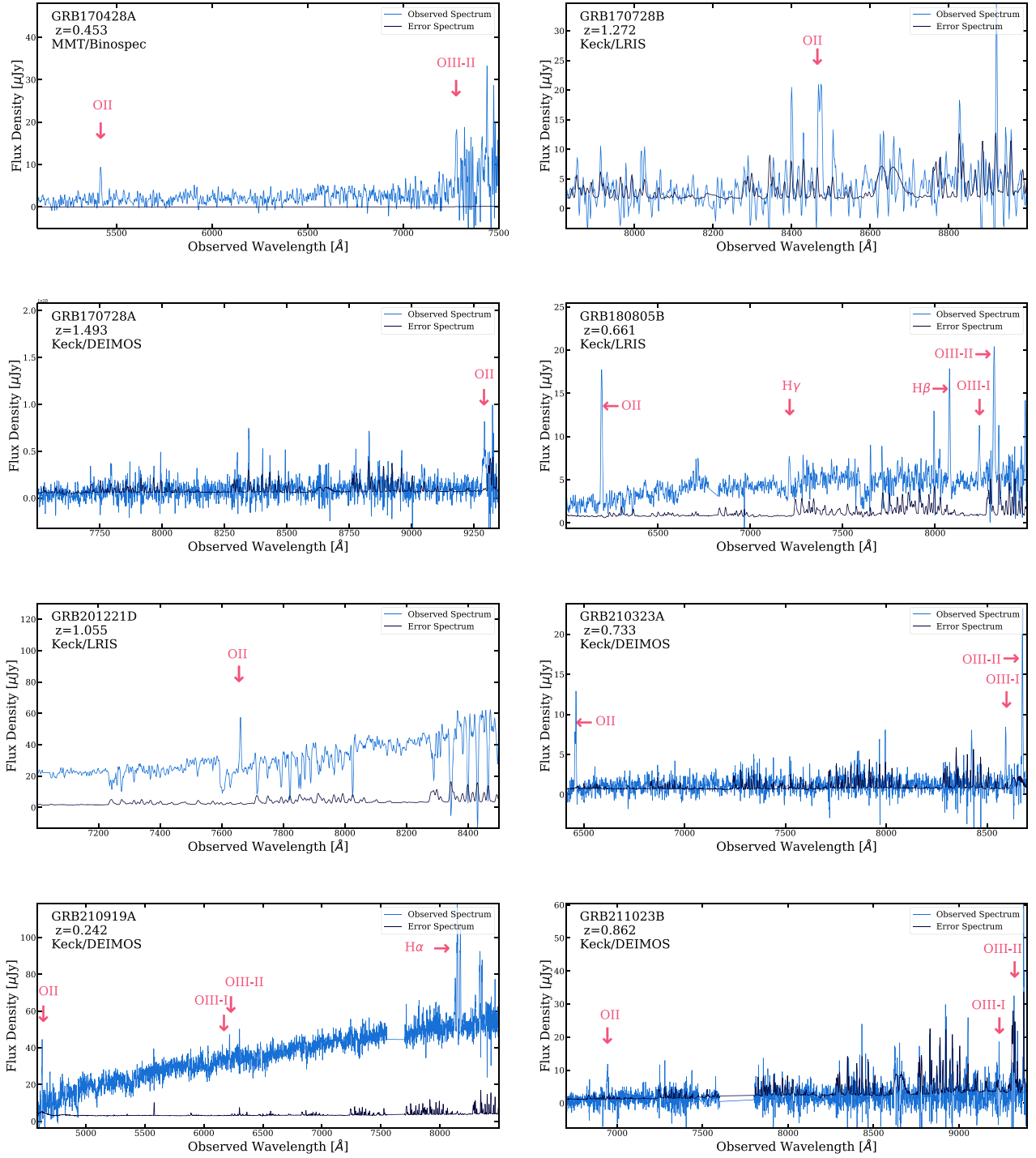


Figure 4. (Continued.)

## 6. Galactocentric Offsets

### 6.1. Angular, Physical, and Host-normalized Offsets

With imaging, host identifications, and redshifts in hand, we now turn to the locations of short GRBs with respect to their hosts. In the context of their NS merger progenitors, offsets are an observable diagnostic for a combination of progenitor kicks and delay times (e.g., Zevin et al. 2020). To determine the position of each GRB relative to its host galaxy, and thus measure precise offsets, we perform relative astrometry by aligning each of the afterglow discovery images to the host galaxy imaging. We

consider three sources of uncertainty in the offsets: the afterglow centroid ( $\sigma_{\text{GRB}}$ ), the astrometric tie uncertainty between the afterglow discovery and the host images ( $\sigma_{\text{GRB} \rightarrow \text{host}}$ ), and the host galaxy centroid uncertainty ( $\sigma_{\text{host}}$ ). We perform the astrometric tie in the same manner as described in Section 4.1. To determine the host centroid uncertainty, we again use `SExtractor`, and find a range of values,  $\sigma_{\text{gal}} \approx 1\text{--}50$  mas. This is generally the smallest source of uncertainty.

For each galaxy/filter combination, we first use the afterglow and host position to measure angular offsets ( $\delta R$ ). The offsets and accompanying combined uncertainties are listed in Table 4. To

**Table 4**  
Short GRB Angular, Physical, and Host-normalized Offsets

GRB	$z$	Afterglow <sup>a</sup>	Offset ( $''$ )	$\sigma$ ( $''$ )	Offset <sup>b</sup> (kpc)	$\sigma$ (kpc)	Offset ( $r_e$ )	$\sigma$ ( $r_e$ )	Reference <sup>c</sup>
050509B	0.2248	X	15.10	3.40	55.19	12.43	2.59	0.58	1
050709	0.1607	X	1.35	0.020	3.76	0.056	2.00	0.030	1
050724A	0.254	O	0.68	0.020	2.74	0.080	0.67	0.020	1
050813	0.719	X	5.96	2.34	43.57	17.37	...	...	This work
051210	2.58	X	3.56	2.00	29.08	16.34	5.65	3.17	1
051221A	0.5464	O	0.32	0.030	2.08	0.19	0.89	0.083	1
060121	...	O	0.119	0.046	0.97	0.37	0.18	0.069	1
060313	...	O	0.32	0.068	2.60	0.55	1.39	0.30	1
060614	0.125	O	0.31	0.35	0.70	0.79	0.86	0.97	This work
060801	1.131	X	1.23	1.31	10.25	10.92	...	...	2
061006	0.461	O	0.24	0.05	1.39	0.29	0.37	0.077	1
061210	0.4095	X	2.82	2.61	15.51	14.36	...	...	3
070429B	0.902	X	0.76	1.7	6.00	13.44	1.17	2.62	3
070707	...	O	0.4	0.03	3.25	0.24	1.11	0.083	3
070714B	0.923	O	1.55	0.11	12.33	0.87	5.17	0.37	3
070724A	0.457	O	0.94	0.03	5.52	0.18	1.49	0.048	3
070729	0.52	X	3.13	2.3	19.72	14.49	...	...	This work
070809	0.473	O	5.70	0.46	34.11	2.75	9.34	0.75	3
071227A	0.381	O	2.80	0.05	14.74	0.26	3.08	0.055	3
080123	0.495	X	8.74	1.25	53.63	7.67	...	...	This work
080503	...	O	0.9	0.03	7.31	0.24	3.46	0.12	3
080905	0.1218	O	8.29	0.08	18.30	0.18	4.61	0.044	3
081226A <sup>d</sup>	...	O	<0.5	...	<4.06	...	...	...	4
090305A	...	O	0.43	0.030	3.49	0.24	1.19	0.083	3
090426A	2.609	O	0.060	0.030	0.49	0.24	0.29	0.14	3
090510	0.903	O	1.33	0.37	10.51	2.92	1.66	0.46	3
090515	0.403	O	13.98	0.03	76.19	0.16	13.98	0.03	3
091109B	...	O	0.52	0.05	4.22	0.41	1.93	0.19	This work
100117A	0.914	O	0.17	0.04	1.35	0.32	0.61	0.14	2
100206A	0.407	X	4.59	2.37	25.28	13.05	...	...	This work
100625A	0.452	X	0.45	1.16	2.63	6.77	...	...	This work
101219A	0.718	X	0.75	0.91	5.48	6.65	...	...	This work
101224A	0.454	X	2.18	2.31	12.75	13.51	...	...	This work
111117A	2.211	X	1.25	0.2	10.52	1.68	...	...	This work
120305A	0.225	X	4.967	1.44	18.09	5.25	...	...	This work
120804A	1.05	O	0.27	0.15	2.22	1.23	...	...	This work
121226A	1.37	X	0.27	1.07	2.31	9.15	...	...	This work
130515A	0.8	X	8.05	1.81	61.22	13.77	...	...	This work
130603B	0.3568	O	1.07	0.04	5.40	0.20	0.71	0.027	3
130716A	2.2	X	3.93	1.69	33.08	14.23	...	...	This work
130822A	0.154	X	22.32	1.82	60.09	4.90	...	...	This work
130912A	...	O	0.48	0.13	3.90	1.06	1.41	0.38	This work
131004A	0.717	O	0.11	0.030	0.80	0.22	0.25	0.068	This work
140129B	0.43	O	0.31	0.31	1.76	1.76	...	...	This work
140622A	0.959	X	4.1	1.4	32.95	11.25	...	...	This work
140903A	0.351	O	0.18	0.02	0.90	0.10	...	...	This work
140930B	1.465	O	1.12	0.5	9.62	4.30	...	...	This work
141212A	0.596	R	2.782	1.823	18.75	12.29	...	...	This work
150101B	0.134	O	3.07	0.030	7.36	0.072	0.78	0.0076	5, This work
150120A	0.46	X	0.81	1.094	4.77	6.44	...	...	This work
150424A	...	O	0.42	0.04	3.41	0.32	1.5	0.14	This work
150728A	0.461	X	1.28	3.44	7.52	20.29	...	...	This work
150831A	1.18	X	1.48	1.18	12.43	9.90	...	...	This work
151229A	0.63	X	1.18	0.88	8.16	6.05	...	...	This work
160303A	1.01	O	1.88	0.11	15.31	0.90	3.42	0.2	This work
160408A	1.9	O	1.65	0.15	14.13	1.25	...	...	This work
160411A	0.82	O	0.18	0.3	1.40	2.30	...	...	This work
160525B	0.64	X	0.79	1.06	5.50	7.38	...	...	This work
160601A	...	O	0.17	0.5	1.38	4.06	...	...	This work
160624A	0.4842	X	1.59	1.03	9.63	6.24	2.37	1.54	This work
160821B	0.1619	O	5.61	0.01	15.74	0.03	4.24	0.008	This work
161001A	0.67	X	2.61	0.88	18.54	6.22	...	...	This work
161104A	0.793	X	0.219	2.19	1.66	16.60	...	...	6

**Table 4**  
(Continued)

GRB	$z$	Afterglow <sup>a</sup>	Offset ( $''$ )	$\sigma$ ( $''$ )	Offset <sup>b</sup> (kpc)	$\sigma$ (kpc)	Offset ( $r_e$ )	$\sigma$ ( $r_e$ )	Reference <sup>c</sup>
170127B	2.28	X	1.24	1.63	10.37	13.60	...	...	This work
170428A	0.453	O	1.32	0.58	7.72	3.39	...	...	This work
170728A	1.493	O	3.75	0.35	32.25	3.01	...	...	This work
170728B	1.272	O	0.99	0.30	8.40	2.55	...	...	This work
180418A	1.56	O	0.16	0.04	1.30	0.32	...	...	7
180618A	0.52	O	1.54	0.27	9.70	1.69	...	...	This work
180727A	1.95	X	0.3	0.6	2.56	5.13	...	...	This work
180805B	0.6612	X	3.44	1.06	24.30	7.49	...	...	This work
181123B	1.754	O	0.59	0.16	5.08	1.38	...	...	8
191031D	1.93	X	1.53	1.25	13.08	10.69	...	...	This work
200219A	0.48	X	1.38	0.88	8.30	5.28	...	...	This work
200411A	0.82	X	4.91	0.88	37.66	6.75	...	...	This work
200522A	0.5536	O	0.143	0.029	0.93	0.19	0.24	0.048	9
200907B	0.56	X	0.37	1.19	2.41	7.78	...	...	This work
201221D	1.055	X	3.57	2.93	29.35	24.09	...	...	This work
210323A	0.733	O	0.8	0.5	5.89	3.68	...	...	This work
210726A	0.37	R	0.044	0.15	0.23	0.78	...	...	This work
210919A	0.2415	O	13.28	0.5	51.05	1.92	...	...	This work
211023B	0.862	O	0.49	0.33	3.84	2.57	...	...	This work
211106A	...	R	0.097	0.036	0.79	0.29	0.49	0.18	10, This work
211211A	0.0763	O	5.44	0.02	7.92	0.029	3.20	0.01	11, This work

**Notes.** Galactocentric offsets for 84 bursts, and one upper limit on the offset (for GRB 081226A). Physical offsets are calculated using the same cosmological parameters across all bursts. For bursts with optical afterglow detections and no publicly available afterglow imaging, we assume an astrometric tie error of  $0''.5$  in our calculation of the offset uncertainty. The positions for bursts with only XRT positions are based on the enhanced XRT positions as of 2022 May (Evans et al. 2009).

<sup>a</sup> Wave band of afterglow used to calculate the offset: X = X-ray, O = Optical, and R = Radio.

<sup>b</sup> For bursts with unknown redshift, physical offsets are calculated for an assumed  $z = 1$ .

<sup>c</sup> Angular offset measurement references: (1) Fong et al. (2010), (2) Berger et al. (2007), (3) Fong & Berger (2013), (4) Nicuesa Guelbenzu et al. (2012), (5) Fong et al. (2016), (6) Nugent et al. (2020), (7) Rouco Escorial et al. (2021), (8) Paterson et al. (2020), (9) Fong et al. (2021), (10) Laskar et al. (2022), (11) Rastinejad et al. (2022).

<sup>d</sup> An angular offset of  $<0''.5$  is reported in Nicuesa Guelbenzu et al. (2012), but an afterglow position is not.

convert to physical offsets, we use the redshifts in Table 2. The values of angular and physical offsets for 84 short GRBs are listed in Table 4. For bursts with unknown redshift or no redshift information, we assume  $z = 1$ . While the median redshift for the entire population is lower ( $z \approx 0.6$ ), we assume that host galaxies that lack redshift information are at higher redshifts than the median. We also note that the angular diameter distance at  $z \gtrsim 0.5$  is relatively flat, so the exact choice of redshift beyond this value will not have a large effect on the physical offset distribution.

The high angular resolution of HST data enables us to calculate the effective radii,  $r_e$ , and thus host-normalized offsets, which we determine from surface brightness profile fitting. When given the choice, we select the filter that corresponds to the rest-frame optical band of the host, as there can be small size differences between filters. We use the IRAF/ellipse routine to generate elliptical intensity isophotes and construct one-dimensional radial surface brightness profiles for the most probable host galaxy for each burst. For each observation, we allow the center, ellipticity, and position angle of each isophote to vary. Using a  $\chi^2$ -minimization grid search, we fit each profile with a Sérsic model with three free parameters: Sérsic index  $n$  (Ciotti & Bertin 1999), the effective radius ( $r_e$ , also known as the half-light radius), and the effective surface brightness ( $\Sigma_e$ ). A single Sérsic component provides an adequate fit ( $\chi^2_\nu \approx 0.4$ – $1.5$ ) for most of the host galaxies. We perform this analysis for the hosts of 10 short GRBs with HST data that do not already have half-light radii measurements determined in this same manner.

Finally, we compile offset measurements for 32 short GRBs with ground-based or HST data (Bloom et al. 2007; Fong et al. 2010, 2016, 2021; Nicuesa Guelbenzu et al. 2012; Fong & Berger 2013; Nugent et al. 2020; Paterson et al. 2020; Rouco Escorial et al. 2021; Laskar et al. 2022; Rastinejad et al. 2022). We recalculate the physical and host-normalized offsets and uncertainties using the best-fit redshifts and the same cosmological parameters as used in this work. We also assume  $z = 1$  for bursts with unknown redshift, and use updated, enhanced XRT positions for bursts in which the most precise position comes from the X-ray afterglow (Goad et al. 2007; Evans et al. 2009). These combined corrections result in minor revisions to the originally published values and are listed in Table 4.

We show all of the physical offsets of 84 short GRBs in Figure 5, with each short GRB’s host galaxy center represented by the origin. While the majority of short GRBs occur at  $\lesssim 10$  kpc and drive the median of  $\approx 7.7$  kpc (Section 6.2), a substantial fraction occur outside of this galactocentric radius.

## 6.2. Offset Distributions

We now combine the distribution for 84 short GRBs, which are all events for which offset measurements are available. This sample includes 34 short GRBs that have enough information for host-normalized offsets. Due to the inclusion of both XRT-localized and subarcsecond localized bursts, the measurement uncertainties vary significantly across the population and have an impact on the offset distribution. Thus, it is imperative to

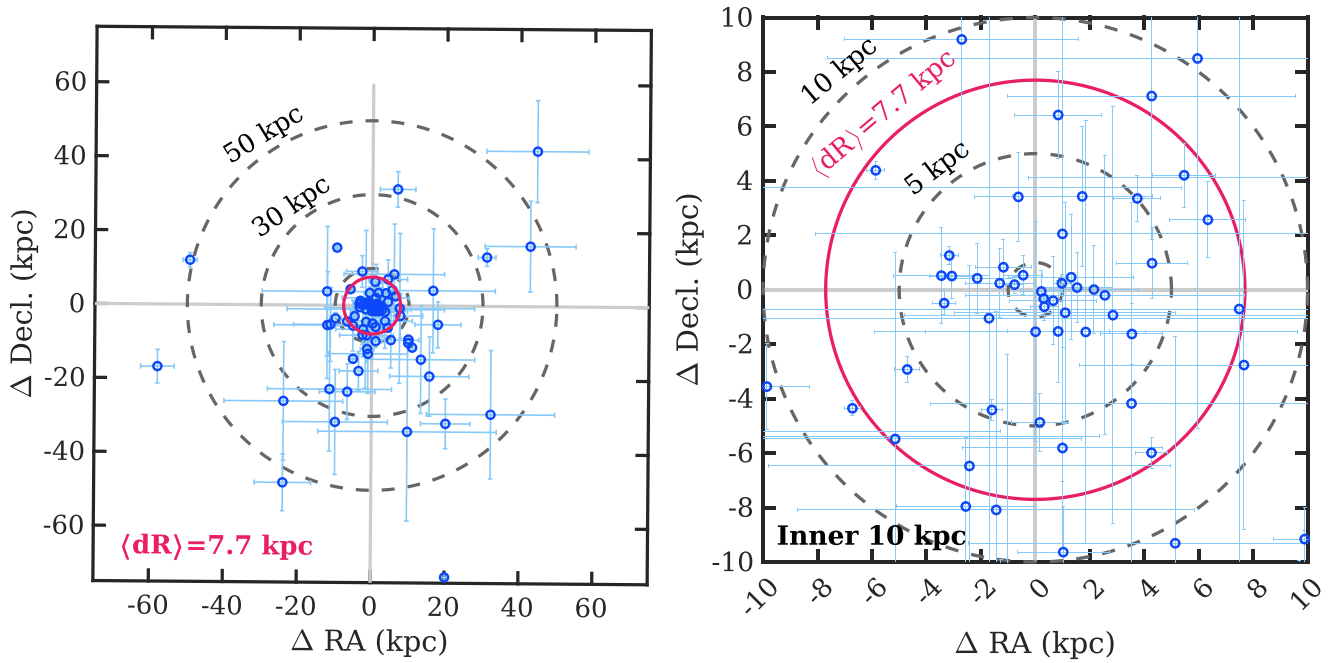


**Figure 5.** Left: the locations of 84 short GRBs with respect to their host galaxy centers (represented by the origin), where uncertainties on individual measurements correspond to  $1\sigma$  confidence. The axes are oriented with north up and east to the left, and the scale is in the frame of the host galaxy (in which negative values correspond to east and/or south of the galaxy). Concentric dashed circles denote 10, 30, and 50 kpc offsets, while the red circle denotes the median on the full distribution of 7.7 kpc. Right: same as left panel, but for only the inner 10 kpc from the host galaxy centers. The panels demonstrate that while most short GRBs reside at  $\lesssim 10$  kpc from their host galaxies, a significant fraction lie outside of this galactocentric radius.

take these uncertainties into account in the final distribution. Indeed, driven largely by the few arcsecond-size XRT positions, 15 short GRBs are in the regime in which the measurement uncertainty is larger than the offset.

To account for these uncertainties and the fact that offsets must be a positive definite value, we use the Rice distribution for each short GRB given their offset and  $1\sigma$  uncertainty. We randomly sample from the resulting distributions 500 times, using the method described in Blanchard et al. (2016). In particular, we use Equation (2) in Blanchard et al. (2016) for the Rice distribution, and note that when  $\delta R/\sigma_{\delta R} > 5$ , the Rice distribution is the same as a Gaussian distribution. We then build 500 cumulative distribution functions (CDFs) and compare them against the observed offsets. Since the CDFs are built from the random samples, the sampled distributions overall have larger physical offsets than the observed distribution since they are driven by the larger uncertainties. We show the distributions of angular, physical, and host-normalized offsets in Figures 6 and 7.

For the observed distribution, we calculate a median of  $1''.23$   $[-0''.96, +3''.30]$  (16th and 84th percentiles on the full distribution) or  $1''.43$   $[-1''.11, +4''.01]$  for the sampled distributions. For the physical offset distribution, we find an observed median of 7.72 kpc with an interval on the full distribution of  $[-6.05, +20.91]$  kpc, or  $9.57[-7.48, +22.82]$  kpc for the sampled distributions. We note that the physical offset distribution includes 11 events with an assumed  $z = 1$ , although the distribution and median minimally change when excluding these events. We find that the short GRBs in the Bronze sample are overall farther from their host galaxies than the Gold or Silver samples (Figure 6); this is to be expected given their less robust associations. Thus, the Gold sample median of  $\approx 4.77$  kpc can be interpreted as a minimum on the short GRB median offset.

Finally, for 34 short GRBs with effective radii measurements, we find medians of  $1.45r_e$   $[-0.93r_e, +2.57r_e]$  ( $1.55r_e$   $[-1.07r_e, +2.71r_e]$ ) for the observed (sampled) distributions. Overall, we find that the observed physical offset distribution here is more extended than determined in previous literature, with a median that is  $\approx 2$ – $3$  kpc higher (Fong et al. 2010; Fong & Berger 2013; O’Connor et al. 2022).

We compare the observed distributions of short GRBs to those of long GRBs (Blanchard et al. 2016), the predicted distributions of field BNS mergers for solar and subsolar metallicities (Wiggins et al. 2018; Figure 6), and the observed distributions of globular clusters in the elliptical galaxy NGC821 (Spitler et al. 2008; Figures 6 and 7). Overall, short GRBs occur at larger offsets than long GRBs, are in reasonable agreement with the expected locations of BNS mergers, and are occur closer to their host galaxies than the observed distributions of globular clusters, in terms of both physical and host-normalized offsets. We further explore the relationship between offset and host galaxy type in Nugent et al. (2022).

## 7. Discussion

### 7.1. Diversifying the Population of Short GRB Hosts: Redshifts, Luminosities, and Offsets

We first address the effects of our methods in defining host galaxy associations. Here, we have adopted a uniform, generous criteria of association, in which every burst with a galaxy in the field that has  $P_{\text{cc},\text{min}} \lesssim 0.2$  is assigned to a host. Realistically, with this method we inevitably inherit some incorrect host assignments when imposing a high  $P_{\text{cc}}$  threshold of 20% for any given association. In particular, we expect  $\lesssim 2\%$  of Gold,  $\lesssim 10\%$  of Silver, and  $\lesssim 20\%$  of Bronze associations to be spurious. This results in an expected total of  $\lesssim 5.7$  incorrect

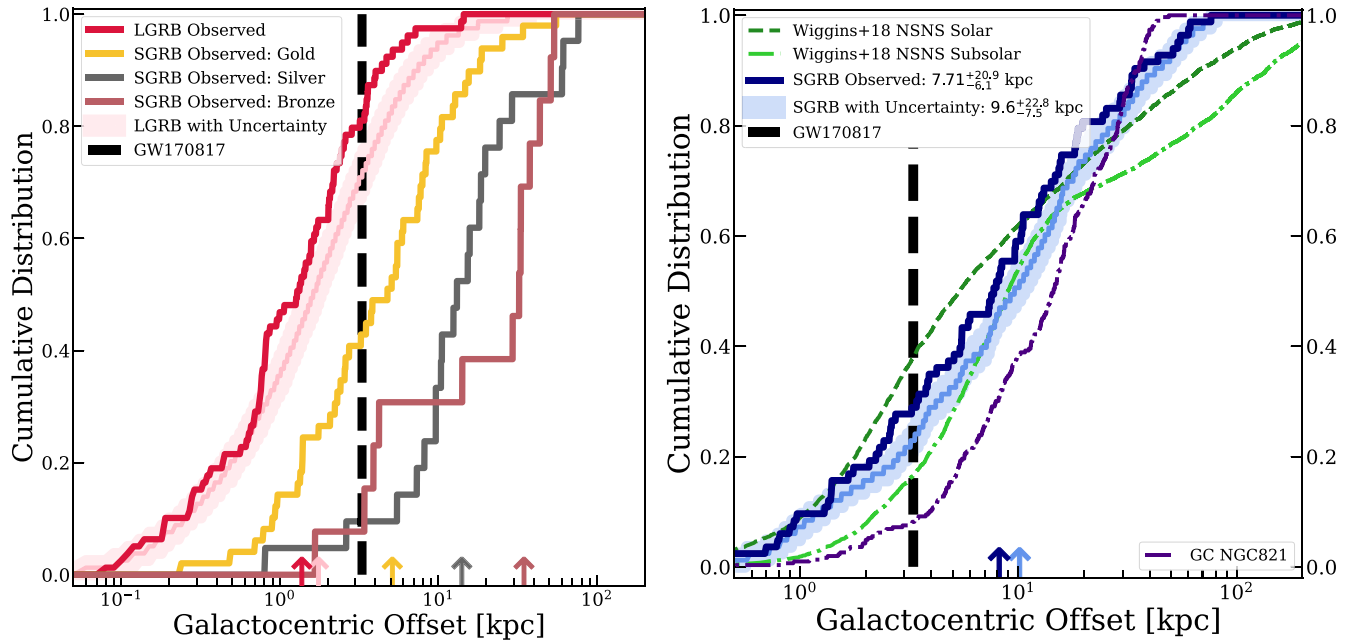


**Figure 6.** Left: the observed physical offset distribution of short GRBs, divided into the Gold, Silver, and Bronze samples; arrows from the bottom denote medians of each distribution. As expected, the bursts with the most tenuous associations (Bronze sample) are farther from their hosts than the Gold and Silver samples. Also shown are the observed offsets of long GRBs and the sampled distributions taking into account uncertainties (red; Blanchard et al. 2016). Right: the observed physical offset distribution of short GRBs (navy blue) and the sampled distributions taking into account measurement uncertainties (shaded light blue). A comparison to representative NS-NS merger models for differing metallicities (dotted and dashed-dotted green lines; Wiggins et al. 2018) shows that the observed and model distributions are overall consistent, although there is a relative dearth of observed high-offset short GRBs. Also shown is the observed distribution of globular clusters in the elliptical galaxy NGC821 (dashed-dotted black line; Spitler et al. 2008); overall, short GRBs are clearly not as extended as this population.

identifications, which is only  $\approx 6.3\%$  of our total sample of associations. On the other hand, by only including the most robust associations (Gold sample,  $P_{\text{cc},\text{min}} \leq 0.02$ ) in short GRB studies, we subject the sample to biases and draw conclusions that may not be reflective of the entire population. Moreover, since the compact object binary progenitors of short GRBs experience natal kicks and thus systemic velocities from their birth sites (e.g., Fryer & Kalogera 1997; Fryer et al. 1999; Belczynski et al. 2006; Vigna-Gómez et al. 2018), it is inevitable that a fraction of events will explode far from their host galaxies, largely irrespective of host brightness. Thus, it is expected that due to the nature of their progenitors and the nature of the  $P_{\text{cc}}$  method, some short GRBs will still have correctly assigned host galaxies with relatively high  $P_{\text{cc}}$  values.

Indeed, we find that by including the less robust host associations (Silver and Bronze), we capture a substantial number of bursts at  $z \gtrsim 1$  (Figure 8). Similarly, we find that the inclusion of the Silver and Bronze hosts results in additional lower-luminosity hosts with  $L_R \lesssim 10^{10} L_{\odot}$  (Figure 9). Finally, the locations of the most robustly associated short GRBs (Gold) are on average 3 kpc closer to their host galaxies than the sample including all associations ( $\approx 4.8$  kpc versus  $\approx 7.7$  kpc; Figure 6). To summarize, we find that establishing a generous association criteria helps to capture more bursts at larger offsets, as well as higher-redshift ( $z \gtrsim 1$ ) and lower-luminosity hosts. While this may come at a cost of incorrect host assignments at the level of  $\lesssim 7\%$ , we note that the Gold sample still comprises over half of the host associations. It is also the subsample with the most information (e.g., redshifts, host-normalized offsets) so these bursts still dominate the distributions in every property. Overall, it is clear that including more associations results in a diversification of the known population of short GRB hosts. In terms of drawing physical

conclusions for their progenitors, we further explore the effect of host associations on stellar population properties in Nugent et al. (2022).

We next explore the effects of including photometric redshifts (the full modeling methods go hand in hand with the stellar population properties, and are thus described in detail in Nugent et al. 2022). Figure 8 shows that the inclusion of a large sample of photometric redshifts also captures higher-redshift events. Indeed, for  $z \gtrsim 1$ , we find that there is a steep drop-off in spectroscopic redshifts, and in turn, a higher frequency of bursts with photometric redshifts (Figure 8). This is in part due to the so-called *redshift desert* in which the most prevalent optical spectral features for redshift identification are shifted into the NIR band where ground-based spectroscopy is less sensitive. At these redshifts, the apparent faintness of the host galaxies also precludes high S/N spectroscopy and only photometric redshifts are possible. In short, including short GRB hosts with photometric redshifts helps fill out the short GRB redshift distribution at  $z \gtrsim 1$ .

This population is particularly important for constraining the functional form of the delay time distribution (DTD). Indeed, Wanderman & Piran (2015) and Paterson et al. (2020) found that even a few short GRBs at  $z \gtrsim 1.5$  could rule out log-normal DTD models to high confidence, whereas power-law DTD models could accommodate tens of events within the Swift short GRB population at  $z \gtrsim 1$ . Here, we find that  $\approx 23\%$  of bursts with known redshift have  $z \gtrsim 1$ , while  $\approx 12\%$  have  $z \gtrsim 1.5$ . As not all bursts have associations or redshifts, these likely represent lower limits on the fractions. Indeed, 10 bursts with identified hosts are too faint to have determined redshifts, while six events have inconclusive host associations. In the extreme case that all 16 of these events are at  $z > 1$  or  $z > 1.5$  in similar proportions to the sample with known redshifts, then as

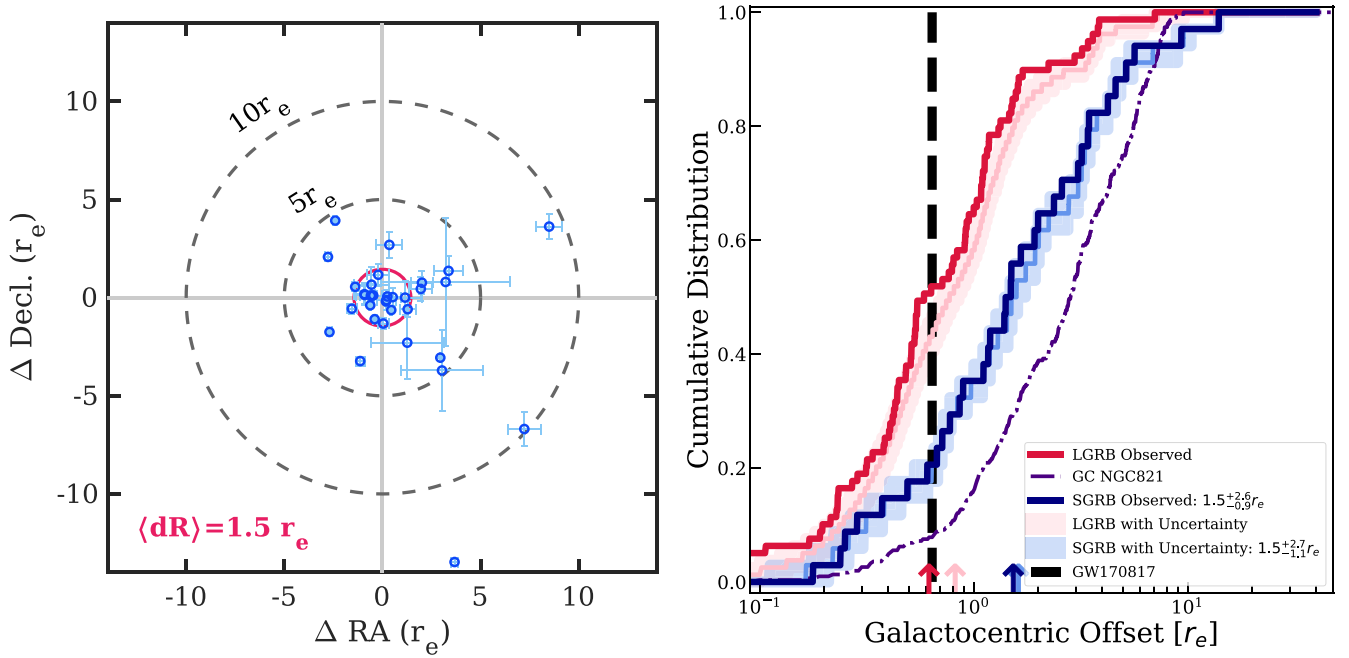


**Figure 7.** Left: the host-normalized offsets of 34 short GRBs with respect to their host galaxy centers (represented by the origin), where uncertainties on individual measurements correspond to  $1\sigma$  confidence. The axes are oriented with north up and east to the left, and the scale is in the frame of the host galaxy (in which negative values correspond to east and/or south of the galaxy). Concentric dashed circles denote  $1r_e$ ,  $5r_e$ , and  $10r_e$  offsets, while the red circle denotes the median on the full distribution of  $1.5r_e$ . Right: the observed distribution of host-normalized offsets for short GRBs (blue solid line) and the sampled distributions with uncertainties (blue shaded region). Also shown are the corresponding distributions of long GRBs (red; Blanchard et al. 2016) and globular clusters in the elliptical galaxy NGC821 (Spitler et al. 2008; dashed-dotted black line). Overall, short GRBs are farther from their hosts than long GRBs but closer than globular clusters, even when normalized by their host galaxy sizes.

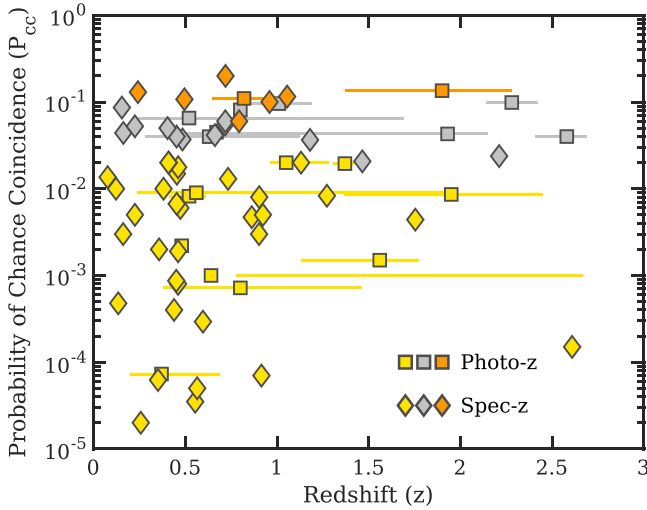


**Figure 8.** Probability of chance coincidence vs. redshift for the host associations in our sample, color coded by classification as Gold (yellow), Silver (gray), or Bronze (orange). Diamonds denote spectroscopic redshifts while squares represent photometric redshifts. Error bars correspond to a  $1\sigma$  confidence. As expected, the average  $P_{cc}$  increases with redshift, especially beyond  $z \gtrsim 1$ . Put another way, the robustness of association decreases with increasing redshift. We also note the larger prevalence of photometric redshifts at  $z \gtrsim 1$ . Not shown are host galaxies with unknown redshift (which are largely Bronze classifications and are likely to be low-luminosity hosts or at  $z \gtrsim 1$ ).

many as  $\approx 41\%$  (22%) could reside at  $z > 1$  ( $z > 1.5$ ). In summary, we find that  $\approx 23\%$ – $41\%$  of short GRBs originate at  $z > 1$  whereas  $\approx 12\%$ – $22\%$  originate at  $z > 1.5$ . Our results are in broad agreement with the finding that  $\approx 20\%$ – $50\%$  of short GRBs could reside at  $z > 1$  based on bursts with no identified host galaxies (O’Connor et al. 2022). In Zevin et al. (2022), we

use the full sample of host galaxies with star formation histories, stellar population ages, and stellar masses derived in Nugent et al. (2022) to calculate a power-law DTD with a fairly steep slope of  $\propto t^{-1.8}$  (e.g., more short delay-time systems compared to a canonical  $\propto t^{-1}$  model), commensurate with the larger fraction of bursts at higher redshift reported here.

Using optical magnitudes and redshifts for 73 short GRBs, we find a range of host optical luminosities,  $L_r \approx 1.4 \times 10^8 L_\odot$  to  $\approx 1.2 \times 10^{11} L_\odot$  with a median of  $\langle L_r \rangle \approx 8 \times 10^9 L_\odot$  (Figure 9). This is a factor of  $\approx 2$  lower than the previous medians based on smaller samples of events (Berger 2009, 2014; Fong et al. 2017). This difference can naturally be explained by the inclusion of a larger number of lower-luminosity hosts, some of which are less robust associations compared to the focus of earlier works. The short GRB photometric catalog presented here generally reaches  $m_{\text{lim}} \approx 26$  mag ( $3\sigma$ ), which is sensitive enough to detect  $L_r \lesssim 10^9 L_\odot$  galaxies out to  $z \approx 1$ . Despite this, there is a lack of short GRB hosts with  $L_r \lesssim 10^9 L_\odot$  when compared to the field galaxy sample from the COSMOS2015 survey (Laigle et al. 2016). Although such galaxies are more common in the universe, this is likely due to the fewer numbers of stars, and thus BNS progenitors, in these galaxies, and goes hand in hand with the lack of low-mass short GRB hosts (Nugent et al. 2022).

We also compare the short GRB population to a sample of 85 long GRB hosts at  $z \lesssim 3$  (Savaglio et al. 2009; Svensson et al. 2010; Hjorth et al. 2012; Vergani et al. 2015; Blanchard et al. 2016). Long GRBs are known to originate from massive star progenitors and overall explode in lower-luminosity host galaxies (Savaglio et al. 2009; Svensson et al. 2010). Figure 9 shows that while there is substantial overlap in the observed host luminosity functions, there are more long GRB hosts with  $L_r \lesssim 10^9 L_\odot$  compared to almost none for the short GRB host

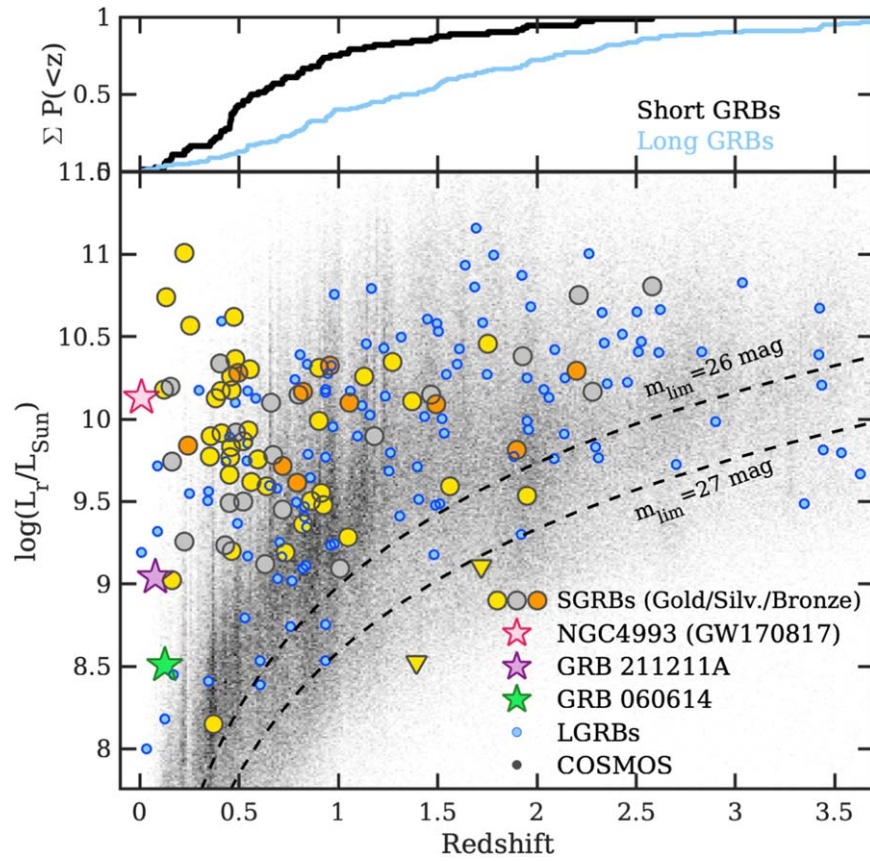


**Figure 9.** Bottom:  $r$ -band host luminosities vs. redshift for 73 short GRBs with redshifts and  $r$ -band magnitudes color coded by Gold, Silver, and Bronze samples (circles). Two bursts with limits on a coincident host and known redshifts from their afterglows are also shown (gold triangles). Approximate limits of the ground-based catalog ( $m_{\text{lim}} \approx 26$  mag) and HST sample ( $m_{\text{lim}} \approx 27$  mag) are plotted as dashed lines. For the subset of bursts that lack a coincident host to  $\gtrsim 27$  mag, these searches are sensitive enough to rule out the faint end of the observed short GRB host luminosity function to  $z \approx 2$ , as well as the fainter end of the field galaxy population (grayscale; COSMOS; Laigle et al. 2016). Also shown are 85 long GRB host luminosities over the same redshift range (black circles; Savaglio et al. 2009; Svensson et al. 2010; Hjorth et al. 2012; Vergani et al. 2015; Blanchard et al. 2016), the host galaxy of the long GRB 211211A which has a likely kilonova (purple star; Rastinejad et al. 2022), the host galaxy of the possible short GRB-EE, GRB 060614 (green star; Gal-Yam et al. 2006), and the host of GW170817, NGC4993 (red star). Overall, short GRB hosts exist in more luminous galaxies than long GRBs at the same redshifts (although there is substantial overlap in their luminosity functions). Top: cumulative distribution of redshifts for short (black) and long (blue) GRBs.

population. Indeed, there are only two short GRB hosts with  $L_r \lesssim 10^9 L_\odot$  compared to 10 long GRB hosts. When compared to the short GRB host population, the host galaxies of long-duration GRB 211211A and the possible short GRB-EE GRB 060614 are among the least luminous galaxies compared to the short GRB host sample. On the other hand, NGC4993 (the host galaxy of GW170817) is more typical of short GRB hosts, albeit older and more quiescent (see, Nugent et al. 2022).

For the six hosts with Inconclusive associations, two have known redshifts from their afterglows (GRBs 150423A and 160410A). The limits on coincident hosts for these bursts are deep enough to rule out hosts down to  $L_r \approx 10^{8.5} - 10^9 L_\odot$  (Figure 9). For the remaining four Inconclusive bursts, the limits are deep enough to detect the faintest known short GRB hosts to  $z \approx 2.5$ . Thus, these bursts either originate from hosts with particularly low luminosities or are highly offset from hosts that are closer to the median.

In terms of galactocentric offsets, the hosts with the most robust associations can be taken as a minimum distribution. Compared to other studies that determined a median of  $\approx 5$ – $6$  kpc (Fong et al. 2010; Fong & Berger 2013; O’Connor et al. 2022), our median value for the entire population is larger, with  $\approx 7.7$  kpc. This is largely because previous studies focused on the most robust associations (e.g., the Gold sample);

indeed, we find a smaller median of  $\approx 4.8$  kpc for this sample alone. In keeping with previous work, we find that short GRBs are also  $\approx 6$  times larger in physical offsets than long GRBs, and  $\approx 2.5$  times larger in host-normalized offsets. This is consistent with the migratory ability of short GRB progenitors and their long delay times, compared to the young and relatively stationary massive star progenitors of long GRBs. Compared to NS merger models, we also find a dearth of observed highly offset ( $\gtrsim 30$  kpc) SGRBs (Figure 6). This can be reconciled if most of the Inconclusive associations originate from hosts at large offsets (as opposed to from low-luminosity, spatially coincident hosts).

Early work suggested that dynamical channels in globular clusters could form BNS mergers and be responsible for  $\approx 30\%$  of observed short GRBs (Grindlay et al. 2006). However, more recent globular cluster simulations have shown the rate of BNS and NSBH mergers to be negligible in clusters compared to the field (Ye et al. 2020). This is corroborated by the lack of a globular cluster to deep limits at or proximal to the position of the BNS merger GW170817 (Lamb et al. 2019b; Fong et al. 2019; Kilpatrick et al. 2022). Indeed, when we compare to the globular cluster distributions, we find that at most  $\lesssim 10\%$  of observed short GRBs could originate from globular clusters in situ.

We finally examine whether or not short GRB-EE or possible short GRB-EE events are distinct in their properties. The mechanism powering the extended emission is uncertain, although has been proposed to be linked to protomagnetar winds (Bucciantini et al. 2012), two-component jets (Barkov & Pozanenko 2011), or a progenitor-specific phenomenon such as NS-BH merger origins (Troja et al. 2008; Gompertz et al. 2020). Equipped with a large sample of short GRBs, we now examine this question in further detail, here and in Nugent et al. (2022). For the 14 short GRB-EE bursts with optical luminosities and magnitudes, we find that these bursts span the full range in host luminosity with a median of  $\langle L_{r,EE} \rangle \approx 1.0 \times 10^{10} L_{\odot}$ , virtually indistinguishable from the classical short GRB sample. We also find a clear lack of correlation with any galaxy-scale environmental property (e.g., stellar population age, stellar mass; Nugent et al. 2022). In terms of locations, Troja et al. (2008) claimed that short GRB-EE events lie closer to their host galaxies than classical short GRBs, and likely arise from NS-BH mergers; this was tentatively supported in Gompertz et al. (2020) although the latter works find their host-normalized offsets to be indistinguishable. Here, we perform an Anderson–Darling (AD) test between these two populations to test the null hypothesis that their projected physical (host-normalized) offsets are drawn from the same underlying distribution. We calculate a  $p$ -value of  $p = 0.25$  ( $p = 0.25$ ). Thus, we cannot rule out the null hypothesis in both cases, and find that these two populations are statistically indistinguishable in terms of the locations with respect to their hosts. We note that if the observed population of short GRB-EE events arise from different progenitors than classical short GRBs, these differences are not manifested as a distinct set of environmental properties.

### 7.2. Selection Effects and Assessing Potential Contamination to Sample

Here, we address the selection effects of our sample born out of the required inclusion criteria, and assess the potential contamination from events that originate from collapsars (e.g., *traditional* long GRBs). First and foremost, robust host galaxy identifications require localization via the detection of afterglows. The brightness of the afterglow depends on a combination of kinetic energy and circumburst density (e.g., Granot & Sari 2002). Thus, the requirement of a detected afterglow might translate to a missing population of bursts at large offsets in the galaxy halos or IGM, or in quiescent galaxies for which the average ISM densities are lower (Perna et al. 2022). Indeed, Figure 6 shows that the predicted spatial distributions of BNS mergers expect  $\approx 20\%$  of the population to reside at  $\gtrsim 50$  kpc (Wiggins et al. 2018). We briefly quantify how many bursts we could be missing at larger offsets. In our study, the requirement for the detection of an afterglow reduces the total available sample by  $\approx 28\%$ . However, the majority ( $\approx 70\%$ ) of the events that lack X-ray afterglows have delayed XRT follow-up observations, either due to observatory constraints or discoveries in BAT ground analysis, whereas only a couple of events in our well-localized sample had delayed X-ray follow-up. Thus, most of the events which lack X-ray afterglows are not likely to have systematically fainter X-ray afterglows than the rest of the population. This leaves  $\approx 12$  events with presumably fainter X-ray afterglows that resulted in afterglow non-detections. If these events indeed went undetected as a result of lower circumburst densities and

larger offsets, their inclusion in this sample would have an effect of  $\lesssim 10\%$ . While the optical afterglows of highly offset bursts have been found to be fainter (Berger 2010), a more recent study exploring the X-ray afterglows did not find any correlation between offset and X-ray afterglow brightness (O’Connor et al. 2022). In summary, we do not expect the population missing at large offsets to be substantial.

Our second major criteria for selection is based on the observed gamma-ray duration ( $T_{90}$ ). The duration-based classification has been shown to be a detector-specific and imperfect delineation between NS merger and collapsar events (Bromberg et al. 2013; Jespersen et al. 2020), and thus we expect to inherit some contamination in our sample. This is rooted in a few examples in which the duration does not provide a one-to-one mapping to the progenitor. For instance, the Fermi short GRB 200826A had a duration of  $\approx 1.1$  s (30–500 keV), but has a photometric excess fully consistent with an associated SN, indicative of a massive star (non-NS merger) origin (Ahumada et al. 2021). Similarly, the Swift and Fermi long GRB 211211A was found to have a photometrically identified kilonova, consistent with an NS merger origin (Rastinejad et al. 2022). To assess the degree of potential contamination by true collapsar events, we apply both the Bromberg et al. (2013) and Jespersen et al. (2020) criteria to our sample, and subsequently search for any systematic variations between bursts classified as collapsars via the various schemes. Bromberg et al. (2013) determine the probability of a given burst arising from a collapsar based on the number counts of bursts at a given duration, and the expectation of a plateau in durations corresponding to the breakout time from a collapsar. They critically conclude that spectral hardness is, if anything, a more important tool for distinction than duration. They subsequently provide a route for the determination of the collapsar probability as a function of duration, as well as in different spectral hardness bins ( $f_{NC}$ ). Since the fit parameters for the spectral hardness bins are not provided directly in Bromberg et al. (2013) we recalculate them based on the provided distributions. Furthermore, we calculate the probabilities based on single power-law spectral fits to the bursts in our sample from the more recent BAT catalog, resulting in some small (typically not important) discrepancies between our values and those in Bromberg et al. (2013). For Jespersen et al. (2020) we directly determine bursts that are either in the short or long category. In this case, Jespersen et al. (2020) used a machine-learning approach to identify features that distinguish short and long GRBs, and these appear to provide a cleaner separation than duration alone. However, they also cannot perform this analysis on bursts of very short duration, and thus we assign these bursts to the short class. It should also be noted that this classification scheme places some short GRB-EE in the long category, perhaps most notably GRB 060614. Our results are listed in Appendix B.

We can then confront the outcomes of these classification schemes based on gamma-ray properties and examine trends with offsets. The baseline expectation is that true NS merger events will have larger offsets than collapsar contaminants. Bromberg et al. (2013) found that  $\approx 35\%$  of Swift GRBs with  $T_{90} \leq 2$  s could be true collapsars. If these probabilities provide an accurate indication of progenitor, we would overall expect that bursts with larger values of  $f_{NC}$  would have larger offsets. However, we find that both the potential contaminants and the

pure NS merger populations under this scheme have indistinguishable offset distributions and span the full range.

In addition to offsets, we can test if the populations of bursts identified as likely collapsars differ from those identified as mergers (shorts) in other properties. Perhaps most notably these include the redshift and the host-specific star formation rate (the latter of which are reported in Nugent et al. 2022). Since the long GRB population is typically found at higher redshift than the short burst population, we may expect that the collapsar contamination may give rise to the apparent high-redshift short GRBs. Similarly, while short GRBs do arise predominantly from star-forming host galaxies, their specific star formation rates are lower. However, AD tests do not reveal any significant differences between the redshifts or specific star formation rates between our sample split according to the two alternative schemes. Moreover, the classification of Bromberg et al. (2013) predicts that  $\approx 1/3$  of  $z < 0.5$  events in our sample are contaminated by true collapsars but this is at odds with the fact that the large majority of events at these redshifts have strong constraints on associated SN emission. We further find that the distributions between our sample and the classical long GRB sample are quite distinct in several properties, including host luminosities, physical offsets (this work), stellar masses, and star formation rates (Nugent et al. 2022). These vastly different distributions are also at odds with a large contamination fraction by true collapsars, and if true, would require extreme host properties in the contaminating population to reconcile the differences.

Zhang et al. (2009) suggest that a full characterization of the population should include the consideration of multiple physical criteria, including host type, offset, location in high energy correlations, and the presence of SNe as a route of distinction between the two classes of burst which they term type I (mergers) and type II (collapsars). Not all of the ideal information is available for each burst. However, based on the available information, the majority of our sample would be classed as type I, or would be inconclusive.

The lack of apparent differences between the samples when employing different inclusion criteria demonstrates that our duration cut is as efficient as others in identifying true, merger-driven short GRBs. While it is impossible to precisely quantify the contamination, since alternative cuts do not result in significantly different distributions in the core parameters, our physical conclusions are not sensitive to our choice of method of determining what constitutes a short GRB.

## 8. Conclusions

We have presented photometric, spectroscopic, and galactocentric offset catalogs that describe the host galaxies of short GRBs and their locations within them. Our sample comprises 90 events discovered during 2005–2021 primarily discovered by Swift. We have come to the following main conclusions:

1. With 1–11 imaging filters per host galaxy, we newly contribute 274 photometric data points in the optical and NIR bands, reaching depths of  $\approx 24$ –27 mag and  $\approx 23$ –26 mag, respectively. We also present 26 new host galaxy spectra and determine 18 spectroscopic redshifts, spanning  $z \approx 0.15$ –1.6.
2. Including associations previously made in the literature, we report host galaxy associations for 84 events, including 26 new associations. This comprises  $\approx 56\%$

of the total Swift population of short GRBs. For the remaining  $\approx 44\%$  of events for which host associations cannot be made with present data, the large majority have observing constraints or lack X-ray afterglows, precluding meaningful observations for host identifications.

3. Taking into account individual measurement uncertainties, we determine a median projected physical offset of  $\approx 7.7$  kpc (16th–84th percentile on the full distribution of 1.65–28.6 kpc) for 84 bursts which is  $\approx 2$ –3 kpc larger than previously found. For 34 short GRBs with effective radii measurements, we find a median host-normalized offset of  $\approx 1.5r_e$  ( $0.57$ – $4.1r_e$ ), although we note that this population is largely comprised of bursts with the most robust host associations. The physical and host-normalized offset distributions are a factor of  $\approx 6$  and  $\approx 2.5$  times larger than those of long GRBs, respectively.
4. The most robust associations account for over half of host identifications (the Gold sample). The Gold sample bursts generally have more luminous host galaxies, lower redshifts, and smaller offsets than those with less robust host associations (Silver and Bronze samples). Thus, the inclusion of less robust associations, even if risking a small potential loss of integrity at the level of  $\lesssim 7\%$ , is important when drawing conclusions on their progenitors.
5. We find that likely  $\approx 23\%$ – $41\%$  of observed Swift short GRBs originate at  $z > 1$ , whereas 12%–22% originate at  $z > 1.5$ . The true frequency of this population relative to the low-redshift sample provides discriminating power among DTD models, and in particular, the prevalence of shorter delay-time systems.
6. In terms of optical luminosity, NGC4993 (the host galaxy of GW170817) has similar properties to the rest of the host population. However, the host galaxies of possible short GRB-EE 060614 and the potentially merger-driven long GRB 211211A are on the low-luminosity end of the population. Overall the short GRB host population exhibits diversity in terms of intrinsic luminosities and locations.
7. As a population, we find that short GRBs with extended emission (including those tentatively classified as such) and classical short GRBs are statistically indistinguishable in terms of their host galaxy luminosities, projected physical offsets, and host-normalized offsets from their hosts. Thus, if these two populations arise from different progenitors, the progenitors do not select for a distinct set of environmental properties.

The launch of Swift enabled the discovery of the first short GRB afterglows in 2005. This crucially paved the way for the first few host galaxy associations (Berger et al. 2005; Fox et al. 2005; Gehrels et al. 2005; Villanor et al. 2005; Bloom et al. 2006). Thanks to the continued longevity of Swift and concerted efforts over 17 yr to identify as many host galaxies as possible, we now have a legacy sample of 84 host galaxies. This sample serves as a cosmological anchor against which future multimessenger BNS and NSBH merger environments can be compared. In particular, the advent of 3G GW detectors in the next two decades, which will be sensitive to BNS mergers to  $z \approx 1$  and beyond (Evans et al. 2021; Shoemaker et al. 2021; Kalogera et al. 2021), will provide a direct comparison to the short GRB host population. Those bursts without clear host associations with present facilities can be pursued with JWST or the Nancy Grace Roman Space

Telescope to potentially unveil a population of high-redshift ( $z \gtrsim 2$  short GRBs). Using the largest and broadest possible data set currently available, this series of legacy catalogs paves the way for interpretation of short GRB progenitors, such as their inference on their stellar population properties and delay time distributions, and fundamental properties of their compact object binary progenitors.

The Fong Group at Northwestern acknowledges the support of the National Science Foundation under grant Nos. AST-1814782 and AST-1909358, and CAREER grant No. AST-2047919. W.F. gratefully acknowledges the support of the David and Lucile Packard Foundation, the Alfred P. Sloan Foundation, and the Research Corporation for Science Advancement through Cottrell Scholar Award #28284. A.E. N. acknowledges support from the Henry Luce Foundation through a Graduate Fellowship in Physics and Astronomy. Y. D. is supported by the National Science Foundation Graduate Research Fellowship under grant No. DGE-1842165. M.N. is supported by the European Research Council (ERC) under the European Unions Horizon 2020 research and innovation program (grant agreement No. 948381) and by a fellowship from the Alan Turing Institute. R.M. acknowledges the support of the National Science Foundation under award Nos. AST-1909796 and AST-1944985. A.L. is supported by the European Research Council (ERC) under the European Unions Horizon 2020 research and innovation program (grant agreement No. 725246).

This research is based on observations made with the NASA/ESA HST obtained from the Space Telescope Science Institute, which is operated by the Association of Universities for Research in Astronomy, Inc., under NASA contract NAS 526555. These observations are associated with programs #14685, 13830, 14237, and 14357. W. M. Keck Observatory and MMT Observatory access was supported by Northwestern University and the Center for Interdisciplinary Exploration and Research in Astrophysics (CIERA). Some of the data presented herein were obtained at the W. M. Keck Observatory, which is operated as a scientific partnership among the California Institute of Technology, the University of California and the National Aeronautics and Space Administration. The Observatory was made possible by the generous financial support of the W. M. Keck Foundation. Observations reported here were obtained at the MMT Observatory, a joint facility of the University of Arizona and the Smithsonian Institution.

Based on observations obtained at the international Gemini Observatory, a program of NOIRLab, which is managed by the Association of Universities for Research in Astronomy (AURA) under a cooperative agreement with the National Science Foundation on behalf of the Gemini Observatory

partnership: the National Science Foundation (United States), National Research Council (Canada), Agencia Nacional de Investigación y Desarrollo (Chile), Ministerio de Ciencia, Tecnología e Innovación (Argentina), Ministério da Ciência, Tecnologia, Inovações e Comunicações (Brazil), and Korea Astronomy and Space Science Institute (Republic of Korea).

This paper includes data gathered with the 6.5 m Magellan Telescopes located at Las Campanas Observatory, Chile.

The United Kingdom Infrared Telescope (UKIRT) was supported by NASA and operated under an agreement among the University of Hawaii, the University of Arizona, and Lockheed Martin Advanced Technology Center; operations are enabled through the cooperation of the East Asian Observatory. We thank the Cambridge Astronomical Survey Unit (CASU) for processing the WFCAM data and the WFCAM Science Archive (WSA) for making the data available.

This work made use of data supplied by the UK Swift Science Data Centre at the University of Leicester.

The LBT is an international collaboration among institutions in the United States, Italy, and Germany. The LBT Corporation partners are the University of Arizona on behalf of the Arizona University system; Istituto Nazionale di Astrofisica, Italy; LBT Beteiligungsgesellschaft, Germany, representing the Max Planck Society, the Astrophysical Institute Potsdam, and Heidelberg University; the Ohio State University; the Research Corporation, on behalf of the University of Notre Dame, University of Minnesota, and University of Virginia.

This work is based in part on observations made with the Spitzer Space Telescope, which was operated by the Jet Propulsion Laboratory, California Institute of Technology under a contract with NASA.

This research has made use of the HST-COSMOS database, operated at CeSAM/LAM, Marseille, France.

*Facilities:* MMT (Binospec, MMIRS), Magellan:Clay (LDSS3), Magellan:Baade (IMACS, FourStar), UKIRT (WFCAM, UFTI), Keck:I (LRIS, MOSFIRE), Keck:II (DEIMOS), HST (WFC3), LBT (LBC, MODS), Gemini: South (GMOS, FLAMINGOS-2), Gemini:North (GMOS, NIRI), Swift (XRT).

*Software:* PyElt (Prochaska et al. 2020), IRAF (Tody 1986, 1993), SExtractor (Bertin & Arnouts 1996).

## Appendix A Photometric Catalog

Here, we present the 542 photometric data points that make up the photometric catalog. We also list derived host galaxy positions from the available imaging, as described in Section 4.1.

**Table A1**  
Photometric Catalog

GRB	R.A. (J2000)	Decl. (J2000)	Filter	$m_{\text{AB}}$ (AB mag)	Reference
050509B	12 <sup>h</sup> 36 <sup>m</sup> 12. <sup>s</sup> 875	+28°58′ 58″84	<i>u</i>	20.32 ± 0.13	Albareti et al. (2017)
			<i>g</i>	18.52 ± 0.02	Albareti et al. (2017)
			<i>r</i>	17.12 ± 0.01	Albareti et al. (2017)
			<i>i</i>	16.60 ± 0.01	Albareti et al. (2017)
			<i>z</i>	16.25 ± 0.01	Albareti et al. (2017)
			<i>J</i>	16.16 ± 0.14	Skrutskie et al. (2006)
			<i>H</i>	15.84 ± 0.18	Skrutskie et al. (2006)
			<i>K</i>	15.98 ± 0.16	Skrutskie et al. (2006)
			F814W	16.28 ± 0.05	Fong et al. (2010)
			4.5 $\mu\text{m}$	16.99 ± 0.01	This work
			8.0 $\mu\text{m}$	18.10 ± 0.05	This work

**Note.** Host galaxy positions and photometry from the literature and this work that have been incorporated into the BRIGHT catalog. We emphasize that the literature data set is comprehensive for a given host in that we attempt to fill out the SED, but does not include all literature photometry that exists for every host galaxy. For bursts with no identified host,  $3\sigma$  limits at the afterglow position are reported. Photometry is in AB magnitudes and is not corrected for extinction in the direction of the bursts. For photometry from archival surveys, if the values are directly from the catalogs, the survey is referenced. If the values are from publications that performed photometry on survey data, the relevant publication is instead referenced. All positions and photometry are also on the BRIGHT website (<https://bright.ciera.northwestern.edu/>).

Table A1 is published in its entirety in the electronic edition of the *Astrophysical Journal*. A portion is shown here for guidance regarding its form and content. (This table is available in its entirety in machine-readable form.)

## Appendix B

### Burst Classifications

**Table B1**  
Classifications of Events in Our Sample

GRB	$T_{90}$ (s)	This Paper Class <sup>a</sup>	Bromberg et al. (2013) $f_{\text{NC}}$ <sup>b</sup>	Jespersen et al. (2020) Class <sup>c</sup>
050509B	0.024	SGRB	0.94	S <sup>d</sup>
050724A	98	SGRB-EE	...	S
050813	0.38	SGRB	0.61	S
051210	1.3	SGRB	0.81	S
051221A	1.4	SGRB	0.18	S
060313	0.74	SGRB	0.91	S
060614	108.7	Possible SGRB-EE	...	L
060801	0.49	SGRB	0.95	S
061006	129.9	SGRB-EE	...	S
061201	0.76	SGRB	0.91	S
061210	85.3	SGRB-EE	...	S
070429B	0.47	SGRB	0.54	S
070714B	64	SGRB-EE	...	L
070724	0.4	SGRB	0.34	S
070729	0.9	SGRB	0.87	S
070809	1.3	SGRB	0.09	L
071227	142.5	SGRB-EE	...	L
080123	115	Possible SGRB-EE	...	L
080503	170	SGRB-EE	...	L
080905A	1.0	SGRB	0.87	S
081226A	0.4	SGRB	0.57	S
090305A	0.54	SGRB	0.94	S
090426A	1.2	SGRB	0.1	L
090510	5.66	Possible SGRB-EE	0.97	S
090515	0.036	SGRB	0.92	S <sup>d</sup>
091109B	0.3	SGRB	0.97	S
100117A	0.3	SGRB	0.97	S
100206A	0.12	SGRB	0.98	S
100625A	0.33	SGRB	0.97	S
101219A	0.83	SGRB	0.90	S
101224A	0.2	SGRB	0.98	S
110112A	0.5	SGRB	0.29	S
111117A	0.47	SGRB	0.95	S
120305A	0.1	SGRB	0.99	S
120804A	0.81	SGRB	0.36	S
121226A	1.0	SGRB	0.29	L
130515A	0.29	SGRB	0.97	S
130603B	0.18	SGRB	0.98	S
130716A	87.7	Possible SGRB-EE	...	L
130822A	0.04	SGRB	0.76	S <sup>d</sup>
130912A	0.28	SGRB	0.69	S
131004A	1.54	SGRB	0.07	L
140129B	1.36	SGRB	0.08	L
140516A	0.26	SGRB	0.49	S
140622A	0.13	SGRB	0.64	S
140903A	0.3	SGRB	0.45	S
141212A	0.3	SGRB	0.68	S
150101B	0.018	SGRB	0.95	S <sup>d</sup>
150120A	1.2	SGRB	0.10	L
150423A	0.22	SGRB	0.98	S
150424A	81	SGRB-EE	...	...
150728A	0.83	SGRB	0.17	S
150831A	0.92	SGRB	0.88	S
151229A	1.44	SGRB	0.08	L

**Table B1**  
(Continued)

GRB	$T_{90}$ (s)	This Paper Class <sup>a</sup>	Bromberg et al. (2013) $f_{\text{NC}}$ <sup>b</sup>	Jespersen et al. (2020) Class <sup>c</sup>
160303A	5.0	SGRB	0.22	S
160408A	0.32	SGRB	0.92	S
160410A	96	Possible SGRB-EE	...	L
160411A	0.36	SGRB	0.63	S
160525B	0.29	SGRB	0.46	S
160601A	0.12	SGRB	0.98	S
160624A	0.2	SGRB	0.98	S
160821B	0.48	SGRB	0.31	S
160927A	0.48	SGRB	0.95	S
161001A	2.6	SGRB	0.55	L
161104A	0.1	SGRB	0.86	S
170127B	0.51	SGRB	0.95	S
170428A	0.2	SGRB	0.98	S
170728B	47.7	Possible SGRB-EE	...	L
180418A	2.29	Possible SGRB-EE	0.02	L
180618A	47.4	SGRB-EE	...	L
180727A	1.1	SGRB	0.27	L
180805B	122.5	SGRB-EE	...	L
181123B	0.26	SGRB	0.97	S
191031D	0.29	SGRB	0.97	...
200219A	288	SGRB-EE	...	...
200411A	0.22	SGRB	0.98	...
200522A	0.62	SGRB	0.46	...
200907B	0.83	SGRB	0.90	...
201006A	0.49	SGRB	0.54	...
201221D	0.16	SGRB	0.80	...
210323A	1.12	SGRB	0.25	...
210726A	0.39	SGRB	0.61	...
210919A	0.16	SGRB	0.80	...
211023B	1.3	SGRB	0.09	...
211106A	1.75	SGRB	0.99	...
211211A	51.37	Merger-driven LGRB	...	...

#### Notes.

<sup>a</sup> Classification of canonical short GRB (SGRB), short GRB with extended emission (SGRB-EE), or possible short GRB with extended emission (possible SGRB-EE) according to Lien et al. (2016). GRB 211211A is classified as a merger-driven long-duration GRB. The values for  $T_{90}$  are from the Swift BAT3 catalog ([https://swift.gsfc.nasa.gov/results/batgrbcatalog/summary\\_cflux/summary\\_general\\_info/summary\\_general.txt](https://swift.gsfc.nasa.gov/results/batgrbcatalog/summary_cflux/summary_general_info/summary_general.txt)) (Lien et al. 2016).


<sup>b</sup> Probability that a burst is not a collapsar following the methods of Bromberg et al. (2013).

<sup>c</sup> Long GRB (“L”) and short GRB (“S”) classifications following the methods of Jespersen et al. (2020).

<sup>d</sup> These bursts have durations that are too short for the Jespersen et al. (2020) criteria to be applied. For the purposes of our comparative analysis, we classify them as short.

#### ORCID iDs

Wen-fai Fong  <https://orcid.org/0000-0002-7374-935X>  
 Anya E. Nugent  <https://orcid.org/0000-0002-2028-9329>  
 Yuxin Dong  <https://orcid.org/0000-0002-9363-8606>  
 Edo Berger  <https://orcid.org/0000-0002-9392-9681>  
 Kerry Paterson  <https://orcid.org/0000-0001-8340-3486>

Ryan Chornock  <https://orcid.org/0000-0002-7706-5668>  
 Andrew Levan  <https://orcid.org/0000-0001-7821-9369>  
 Peter Blanchard  <https://orcid.org/0000-0003-0526-2248>  
 Kate D. Alexander  <https://orcid.org/0000-0002-8297-2473>  
 Jennifer Andrews  <https://orcid.org/0000-0003-0123-0062>  
 Bethany E. Cobb  <https://orcid.org/0000-0002-9118-9448>  
 Antonino Cucchiara  <https://orcid.org/0000-0001-6455-5660>  
 Derek Fox  <https://orcid.org/0000-0002-3714-672X>  
 Chris L. Fryer  <https://orcid.org/0000-0003-2624-0056>  
 Alexa C. Gordon  <https://orcid.org/0000-0002-5025-4645>  
 Charles D. Kilpatrick  <https://orcid.org/0000-0002-5740-7747>  
 Ragnhild Lunnan  <https://orcid.org/0000-0001-9454-4639>  
 Raffaella Margutti  <https://orcid.org/0000-0003-4768-7586>  
 Adam Miller  <https://orcid.org/0000-0001-9515-478X>  
 Peter Milne  <https://orcid.org/0000-0002-0370-157X>  
 Matt Nicholl  <https://orcid.org/0000-0002-2555-3192>  
 Daniel Perley  <https://orcid.org/0000-0001-8472-1996>  
 Jillian Rastinejad  <https://orcid.org/0000-0002-9267-6213>  
 Alicia Rouco Escorial  <https://orcid.org/0000-0003-3937-0618>  
 Genevieve Schroeder  <https://orcid.org/0000-0001-9915-8147>  
 Nathan Smith  <https://orcid.org/0000-0001-5510-2424>  
 Nial Tanvir  <https://orcid.org/0000-0003-3274-6336>  
 Giacomo Terreran  <https://orcid.org/0000-0003-0794-5982>

## References

- Abbott, B. P., Abbott, R., Abbott, T. D., et al. 2017a, *ApJL*, **848**, L13  
 Abbott, B. P., Abbott, R., Abbott, T. D., et al. 2017b, *PhRvL*, **119**, 161101  
 Abbott, B. P., Abbott, R., Abbott, T. D., et al. 2019, *PhRvX*, **9**, 031040  
 Abbott, B. P., Abbott, R., Abbott, T. D., et al. 2020a, *ApJL*, **892**, L3  
 Abbott, B. P., Abbott, R., Abbott, T. D., et al. 2020b, *LRR*, **23**, 3  
 Agüí Fernández, J. F., Thöne, C. C., Kann, D. A., et al. 2021, arXiv:2109.13838  
 Ahumada, T., Singer, L. P., Anand, S., et al. 2021, *NatAs*, **5**, 917  
 Alam, S., Albareti, F. D., Allende Prieto, C., et al. 2015, *ApJS*, **219**, 12  
 Albareti, F. D., Allende Prieto, C., Almeida, A., et al. 2017, *ApJS*, **233**, 25  
 Audcent-Ross, F. M., Meurer, G. R., Audcent, J. R., et al. 2020, *MNRAS*, **492**, 848  
 Barkov, M. V., & Pozanenko, A. S. 2011, *MNRAS*, **417**, 2161  
 Becker, A. 2015, HOTPANTS: High Order Transform of PSF ANd Template Subtraction, Astrophysics Source Code Library, ascl:1504.004  
 Beckwith, S. V. W., Stiavelli, M., Koekemoer, A. M., et al. 2006, *AJ*, **132**, 1729  
 Belczynski, K., Perna, R., Bulik, T., et al. 2006, *ApJ*, **648**, 1110  
 Bennett, C. L., Larson, D., Weiland, J. L., & Hinshaw, G. 2014, *ApJ*, **794**, 135  
 Berger, E. 2009, *ApJ*, **690**, 231  
 Berger, E. 2010, *ApJ*, **722**, 1946  
 Berger, E. 2014, *ARA&A*, **52**, 43  
 Berger, E., Cenko, S. B., Fox, D. B., & Cucchiara, A. 2009, *ApJ*, **704**, 877  
 Berger, E., Fox, D. B., Price, P. A., et al. 2007, *ApJ*, **664**, 1000  
 Berger, E., Price, P. A., Cenko, S. B., et al. 2005, *Natur*, **438**, 988  
 Berger, E., Zauderer, B. A., Levan, A., et al. 2013, *ApJ*, **765**, 121  
 Bertin, E., & Arnouts, S. 1996, *A&AS*, **117**, 393  
 Blanchard, P. K., Berger, E., Fong, W., et al. 2017, *ApJL*, **848**, L22  
 Blanchard, P. K., Berger, E., & Fong, W.-F. 2016, *ApJ*, **817**, 144  
 Bloom, J. S., Kulkarni, S. R., & Djorgovski, S. G. 2002, *AJ*, **123**, 1111  
 Bloom, J. S., Perley, D. A., Chen, H.-W., et al. 2007, *ApJ*, **654**, 878  
 Bloom, J. S., Prochaska, J. X., Pooley, D., et al. 2006, *ApJ*, **638**, 354  
 Bromberg, O., Nakar, E., Piran, T., & Sari, R. 2013, *ApJ*, **764**, 179  
 Bucciattini, N., Metzger, B. D., Thompson, T. A., & Quataert, E. 2012, *MNRAS*, **419**, 1537  
 Cano, Z., de Ugarte Postigo, A., Malesani, D., & Thoene, C. C. 2016, GCN, **19160**, 1  
 Cardelli, J. A., Clayton, G. C., & Mathis, J. S. 1989, *ApJ*, **345**, 245  
 Castro-Tirado, A. J., Sanchez-Ramirez, R., Lombardi, G., & Rivero, M. A. 2015, GCN, **17758**, 1  
 Cenko, S. B., Berger, E., Nakar, E., et al. 2008, arXiv:0802.0874  
 Chambers, K. C., Magnier, E. A., Metcalfe, N., et al. 2016, arXiv:1612.05560  
 Chornock, R., Fong, W., & Fox, D. B. 2014, GCN, **17177**, 1  
 Chornock, R., Lunnan, R., & Berger, E. 2013, GCN, **15307**, 1  
 Ciotti, L., & Bertin, G. 1999, *A&A*, **352**, 447  
 Covino, S., Malesani, D., Israel, G. L., et al. 2006, *A&A*, **447**, L5  
 Cucchiara, A., Prochaska, J. X., Perley, D., et al. 2013, *ApJ*, **777**, 94  
 D'Avanzo, P., Malesani, D., Covino, S., et al. 2009, *A&A*, **498**, 711  
 De Pasquale, M. 2019, *Galax*, **7**, 30  
 de Ugarte Postigo, A., Kann, D. A., Izzo, L., et al. 2020, GCN, **29132**, 1  
 de Ugarte Postigo, A., Malesani, D., Kruehler, T., et al. 2016, GCN, **19154**, 1  
 de Ugarte Postigo, A., Thöne, C. C., Rowlinson, A., et al. 2014, *A&A*, **563**, A62  
 Della Valle, M., Chincarini, G., Panagia, N., et al. 2006, *Natur*, **444**, 1050  
 Dey, A., Schlegel, D. J., Lang, D., et al. 2019, *AJ*, **157**, 168  
 Evans, M., Adhikari, R. X., Afle, C., et al. 2021, arXiv:2109.09882  
 Evans, P. A., Beardmore, A. P., Page, K. L., et al. 2009, *MNRAS*, **397**, 1177  
 Fazio, G. G., Hora, J. L., Allen, L. E., et al. 2004, *ApJS*, **154**, 10  
 Ferrero, P., Sanchez, S. F., Kann, D. A., et al. 2007, *AJ*, **134**, 2118  
 Flewelling, H. A., Magnier, E. A., Chambers, K. C., et al. 2020, *ApJS*, **251**, 7  
 Fong, W., & Berger, E. 2013, *ApJ*, **776**, 18  
 Fong, W., Berger, E., Blanchard, P. K., et al. 2017, *ApJL*, **848**, L23  
 Fong, W., Berger, E., Chornock, R., et al. 2011, *ApJ*, **730**, 26  
 Fong, W., Berger, E., Chornock, R., et al. 2013, *ApJ*, **769**, 56  
 Fong, W., Berger, E., & Fox, D. B. 2010, *ApJ*, **708**, 9  
 Fong, W., Berger, E., Margutti, R., & Zauderer, B. A. 2015, *ApJ*, **815**, 102  
 Fong, W., Blanchard, P. K., Alexander, K. D., et al. 2019, *ApJL*, **883**, L1  
 Fong, W., Laskar, T., Rastinejad, J., et al. 2021, *ApJ*, **906**, 127  
 Fong, W., Margutti, R., Chornock, R., et al. 2016, *ApJ*, **833**, 151  
 Fox, D. B., Frail, D. A., Price, P. A., et al. 2005, *Natur*, **437**, 845  
 Fruchter, A. S., Levan, A. J., Strolger, L., et al. 2006, *Natur*, **441**, 463  
 Fryer, C., & Kalogera, V. 1997, *ApJ*, **489**, 244  
 Fryer, C. L., Woosley, S. E., & Hartmann, D. H. 1999, *ApJ*, **526**, 152  
 Fynbo, J. P. U., Watson, D., Thöne, C. C., et al. 2006, *Natur*, **444**, 1047  
 Gaia Collaboration, Brown, A. G. A., Vallenari, A., et al. 2018, *A&A*, **616**, A1  
 Gal-Yam, A., Fox, D. B., Price, P. A., et al. 2006, *Natur*, **444**, 1053  
 Gehrels, N., Chincarini, G., Giommi, P., et al. 2004, *ApJ*, **611**, 1005  
 Gehrels, N., Norris, J. P., Barthelmy, S. D., et al. 2006, *Natur*, **444**, 1044  
 Gehrels, N., Sarazin, C. L., O'Brien, P. T., et al. 2005, *Natur*, **437**, 851  
 Goad, M. R., Tyler, L. G., Beardmore, A. P., et al. 2007, *A&A*, **476**, 1401  
 Goldstein, A., Veres, P., Burns, E., et al. 2017, *ApJL*, **848**, L14  
 Gompertz, B. P., Levan, A. J., & Tanvir, N. R. 2020, *ApJ*, **895**, 58  
 Gorosabel, J., Castro-Tirado, A. J., Guziy, S., et al. 2006, *A&A*, **450**, 87  
 Graham, J. F., Fruchter, A. S., Levan, A. J., et al. 2009, *ApJ*, **698**, 1620  
 Granot, J., & Sari, R. 2002, *ApJ*, **568**, 820  
 Grindlay, J., Portegies Zwart, S., & McMillan, S. 2006, *NatPh*, **2**, 116  
 Hamly, N. C., Collins, R. S., Cross, N. J. G., et al. 2008, *MNRAS*, **384**, 637  
 Hjorth, J., Malesani, D., Jakobsson, P., et al. 2012, *ApJ*, **756**, 187  
 Hjorth, J., Watson, D., Fynbo, J. P. U., et al. 2005, *Natur*, **437**, 859  
 Hogg, D. W., Pahre, M. A., McCarthy, J. K., et al. 1997, *MNRAS*, **288**, 404  
 Jespersen, C. K., Severin, J. B., Steinhart, C. L., et al. 2020, *ApJL*, **896**, L20  
 Jin, Z.-P., Li, X., Cano, Z., et al. 2015, *ApJL*, **811**, L22  
 Jin, Z.-P., Li, X., Wang, H., et al. 2018, *ApJ*, **857**, 128  
 Johnson, B. D., Leja, J., Conroy, C., & Speagle, J. S. 2021, *ApJS*, **254**, 22  
 Kalogera, V., Sathyaprakash, B. S., Bailes, M., et al. 2021, arXiv:2111.06990  
 Kasliwal, M. M., Korobkin, O., Lau, R. M., Wollaeger, R., & Fryer, C. L. 2017, *ApJL*, **843**, L34  
 Kelly, P. L., Kirshner, R. P., & Pahre, M. 2008, *ApJ*, **687**, 1201  
 Kilpatrick, C. D., Fong, W.-f., Blanchard, P. K., et al. 2022, *ApJ*, **926**, 49  
 Kilpatrick, C. D., Malesani, D. B., & Fong, W. 2020, GCN, **29133**, 1  
 Knust, F., Greiner, J., van Eerten, H. J., et al. 2017, *A&A*, **607**, A84  
 Kouveliotou, C., Meegan, C. A., Fishman, G. J., et al. 1993, *ApJL*, **413**, L101  
 Laigle, C., McCracken, H. J., Ilbert, O., et al. 2016, *ApJS*, **224**, 24  
 Lamb, G. P., Lyman, J. D., Levan, A. J., et al. 2019b, *ApJL*, **870**, L15  
 Lamb, G. P., Tanvir, N. R., Levan, A. J., et al. 2019a, *ApJ*, **883**, 48  
 Lang, D., Hogg, D. W., & Schlegel, D. J. 2016, *AJ*, **151**, 36  
 Laskar, T., Rouco Escorial, A., Schroeder, G., et al. 2022, *ApJ*, **935**, L11  
 Leibler, C. N., & Berger, E. 2010, *ApJ*, **725**, 1202  
 Leja, J., Johnson, B. D., Conroy, C., Dokkum, P. G. V., & Byler, N. 2017, *ApJ*, **837**, 170  
 Levesque, E. M., Bloom, J. S., Butler, N. R., et al. 2010, *MNRAS*, **401**, 963  
 Li, W., Chornock, R., Leaman, J., et al. 2011, *MNRAS*, **412**, 1473  
 Lien, A., Sakamoto, T., Barthelmy, S. D., et al. 2016, *ApJ*, **829**, 7  
 Lunnan, R., Chornock, R., Berger, E., et al. 2014, *ApJ*, **787**, 138  
 Lunnan, R., Chornock, R., Berger, E., et al. 2015, *ApJ*, **804**, 90  
 Lyman, J. D., Levan, A. J., Tanvir, N. R., et al. 2017, *MNRAS*, **467**, 1795

- Margutti, R., Berger, E., Fong, W., et al. 2012, *ApJ*, **756**, 63
- Margutti, R., & Chornock, R. 2021, *ARA&A*, **59**, 155
- McBreen, S., Krühler, T., Rau, A., et al. 2010, *A&A*, **516**, A71
- Metcalfe, N., Shanks, T., Weilbacher, P. M., et al. 2006, *MNRAS*, **370**, 1257
- Nicuesa Guelbenzu, A., Klose, S., Greiner, J., et al. 2012, *A&A*, **548**, A101
- Niino, Y., Aoki, K., Hashimoto, T., et al. 2017, *PASJ*, **69**, 27
- Norris, J. P., & Bonnell, J. T. 2006, *ApJ*, **643**, 266
- Nugent, A. E., Fong, W., Dong, Y., et al. 2020, *ApJ*, **904**, 52
- Nugent, A. E., Fong, W., Dong, Y., et al. 2022, arXiv:2206.01764
- O'Connor, B., Troja, E., Dichiaro, S., et al. 2021, *MNRAS*, **502**, 1279
- O'Connor, B., Troja, E., Dichiaro, S., et al. 2022, *MNRAS*, **515**, 4890
- Papovich, C., Shipley, H. V., Mehrtens, N., et al. 2016, *ApJS*, **224**, 28
- Paterson, K., Fong, W., Nugent, A., et al. 2020, *ApJL*, **898**, L32
- Perley, D. A. 2015, GCN, **17744**, 1
- Perley, D. A., Krühler, T., Schulze, S., et al. 2016b, *ApJ*, **817**, 7
- Perley, D. A., Metzger, B. D., Granot, J., et al. 2009, *ApJ*, **696**, 1871
- Perley, D. A., Modjaz, M., Morgan, A. N., et al. 2012, *ApJ*, **758**, 122
- Perley, D. A., Quimby, R. M., Yan, L., et al. 2016a, *ApJ*, **830**, 13
- Perley, D. A., Tanvir, N. R., Hjorth, J., et al. 2016c, *ApJ*, **817**, 8
- Perna, R., Artale, M. C., Wang, Y.-H., et al. 2022, *MNRAS*, **512**, 2654
- Prochaska, J., Hennawi, J., Westfall, K., et al. 2020, *JOSS*, **5**, 2308
- Prochaska, J. X., Bloom, J. S., Chen, H.-W., et al. 2006, *ApJ*, **642**, 989
- Rastinejad, J. C., Fong, W., Kilpatrick, C. D., et al. 2021, *ApJ*, **916**, 89
- Rastinejad, J. C., Gompertz, B. P., Levan, A. J., et al. 2022, arXiv:2204.10864
- Ricker, G. R., Atteia, J.-L., Crew, G. B., et al. 2003, in AIP Conf. Ser. 662, Gamma-Ray Burst and Afterglow Astronomy 2001: A Workshop Celebrating the First Year of the HETE Mission, ed. G. R. Ricker & R. K. Vanderspek (Melville, NY: AIP), **3**
- Rossi, A., Cusano, F., Palazzi, E., et al. 2022, GCN, **31453**, 1
- Rossi, A., Palazzi, E., Amati, L., et al. 2021, GCN, **31107**, 1
- Rouco Escorial, A., Fong, W., Veres, P., et al. 2021, *ApJ*, **912**, 95
- Rowlinson, A., Wiersema, K., Levan, A. J., et al. 2010, *MNRAS*, **408**, 383
- Savaglio, S., Glazebrook, K., & Le Borgne, D. 2009, *ApJ*, **691**, 182
- Savchenko, V., Ferrigno, C., Kuulkers, E., et al. 2017, *ApJL*, **848**, L15
- Schlafly, E. F., & Finkbeiner, D. P. 2011, *ApJ*, **737**, 103
- Schlegel, D., Dey, A., Herrera, D., et al. 2021, AAS Meeting Abstracts, **53**, 235.03
- Schulze, S., Yaron, O., Sollerman, J., et al. 2021, *ApJS*, **255**, 29
- Selsing, J., Krühler, T., Malesani, D., et al. 2018, *A&A*, **616**, A48
- Selsing, J., Malesani, D., Goldoni, P., et al. 2019, *A&A*, **623**, A92
- Shoemaker, D. H., Ballmer, S., Barsuglia, M., et al. 2021, arXiv:2112.12718
- Skrutskie, M. F., Cutri, R. M., Stiening, R., et al. 2006, *AJ*, **131**, 1163
- Soderberg, A. M., Berger, E., Kasliwal, M., et al. 2006, *ApJ*, **650**, 261
- Spitler, L. R., Forbes, D. A., Strader, J., Brodie, J. P., & Gallagher, J. S. 2008, *MNRAS*, **385**, 361
- Stratta, G., D'Avanzo, P., Piranomonte, S., et al. 2007, *A&A*, **474**, 827
- Sullivan, M., Le Borgne, D., Pritchett, C. J., et al. 2006, *ApJ*, **648**, 868
- Svensson, K. M., Levan, A. J., Tanvir, N. R., Fruchter, A. S., & Strolger, L.-G. 2010, *MNRAS*, **405**, 57
- Tanvir, N. R., Levan, A. J., Fruchter, A. S., et al. 2015, GCN, **18100**, 1
- Tauris, T. M., Kramer, M., Freire, P. C. C., et al. 2017, *ApJ*, **846**, 170
- Timlin, J. D., Ross, N. P., Richards, G. T., et al. 2016, *ApJS*, **225**, 1
- Tody, D. 1986, *Proc. SPIE*, **627**, 733
- Tody, D. 1993, in ASP Conf. Ser. 52, Astronomical Data Analysis Software and Systems II, ed. R. J. Hanisch, R. J. V. Brissenden, & J. Barnes (San Francisco, CA: ASP), **173**
- Tonry, J. L., Stubbs, C. W., Lykke, K. R., et al. 2012, *ApJ*, **750**, 99
- Troja, E., Castro-Tirado, A. J., Becerra González, J., et al. 2019, *MNRAS*, **489**, 2104
- Troja, E., King, A. R., O'Brien, P. T., Lyons, N., & Cusumano, G. 2008, *MNRAS*, **385**, L10
- Troja, E., Sakamoto, T., Cenko, S. B., et al. 2016, *ApJ*, **827**, 102
- Tunnicliffe, R. L., Levan, A. J., Tanvir, N. R., et al. 2014, *MNRAS*, **437**, 1495
- Ukwatta, T. N., Barthelmy, S. D., Beardmore, A. P., et al. 2016, GCN, **19148**, 1
- van den Bergh, S., Li, W., & Filippenko, A. V. 2005, *PASP*, **117**, 773
- Vergani, S. D., Salvaterra, R., Japelj, J., et al. 2015, *A&A*, **581**, A102
- Vigna-Gómez, A., Neijssel, C. J., Stevenson, S., et al. 2018, *MNRAS*, **481**, 4009
- Villasenor, J. S., Lamb, D. Q., Ricker, G. R., et al. 2005, *Natur*, **437**, 855
- Wanderman, D., & Piran, T. 2015, *MNRAS*, **448**, 3026
- Wenger, M., Ochsenein, F., Egret, D., et al. 2000, *A&AS*, **143**, 9
- Werner, M. W., Roellig, T. L., Low, F. J., et al. 2004, *ApJS*, **154**, 1
- Wiggins, B. K., Fryer, C. L., Smidt, J. M., et al. 2018, *ApJ*, **865**, 27
- Willems, B., Kalogera, V., & Henninger, M. 2004, *ApJ*, **616**, 414
- Wong, T.-W., Willems, B., & Kalogera, V. 2010, *ApJ*, **721**, 1689
- Wright, E. L., Eisenhardt, P. R. M., Mainzer, A. K., et al. 2010, *AJ*, **140**, 1868
- Ye, C. S., Fong, W.-f., Kremer, K., et al. 2020, *ApJL*, **888**, L10
- Zevin, M., Kelley, L. Z., Nugent, A., et al. 2020, *ApJ*, **904**, 190
- Zevin, M., Nugent, A. E., & Adhikari, S. 2022, arXiv:2206.02814
- Zhang, B., Zhang, B.-B., Virgili, F. J., et al. 2009, *ApJ*, **703**, 1696